

Conductive 2D Conjugated Metal–Organic Framework Thin Films: Synthesis and Functions for (Opto-)electronics

Jinxin Liu, Yunxu Chen, Xinliang Feng, and Renhao Dong*

Two-dimensional conjugated metal–organic frameworks (2D c-MOFs), possessing extended π - d conjugated planar structure, are emerging as a unique class of electronic materials due to their intrinsic electrical conductivities. Taking advantage of the large-area flat surface, 2D c-MOF thin films allow facile device integration with sufficient electrode contact, high device stability, and high charge transport, thereby emerging as appealing active layers for a broad range of electronic applications. Synthesis and device investigation of thin films are of great importance for their further development, which are systematically summarized in the current review. Here, the authors firstly introduce the molecular structures of representative 2D c-MOFs and present the fundamental understanding on structure–property relationships. After that, the state-of-art synthetic methodologies toward high-quality 2D c-MOF thin films are summarized, including exfoliation and reassembly (ERA), liquid-interface-assisted synthesis (LIAS), and chemical vapor deposition (CVD). By considering the advantages of 2D c-MOF films in device integration, remarkable progress in (opto-)electronic device applications are discussed, such as field-effect transistors (FETs), chemiresistive sensors, photodetectors, superconductors, and thermoelectrics. In the end, the remained challenges about the development of 2D c-MOF films for (opto-)electronics are highlighted and possible future directions are proposed to address these challenges.

1. Introduction


Metal–organic frameworks (MOFs) with well-defined porosity and structural tunability have attracted extensive research attention in widespread functional applications including catalysis,^[1] separation,^[2] energy storage,^[3] and gas storage.^[4] However, most of the traditional MOFs exhibit low electrical conductivity, which has ultimately restricted their development in electronic devices.^[5] Taking advantage of the extended π - d conjugated planar structure, 2D conjugated MOFs (2D c-MOFs) have been demonstrated as an emerging class of electronic materials,^[6] which exhibit high electrical conductivity up to 10^3 S cm^{-1} .^[7] In addition to the intrinsic electrical conductivities, numerous unique physical properties have also been discovered, such as tailored bandgaps from metal to semiconductor,^[8] high charge mobility,^[9] photo-response,^[10] thermal transport,^[11] and ferromagnetic ordering,^[12] thereby demonstrating their significant potential as active layers for broad (opto-)electronic applications.^[6]

However, the synthesis of 2D c-MOFs has been mostly performed via the hydro-/solvo-thermal method, which generally results in polycrystalline^[13] or single-crystalline bulk samples.^[14] For the (opto-)electronic device integration and measurement, it is required to compress the bulk samples into pellets. In this regard, long-range charge transport could be hindered by the mass of grain boundaries, defects, and gaps between particles,^[15,16] thus leading to complicated charge transport mechanisms and low device performance. A bulk-single-crystal electronic device would be an ideal candidate for discovering the intrinsic transport mechanism and achieving superior performance.^[17] However, it is not trivial to consider the critical challenges originating from limited electrode patterning and large contact resistance. In addition, the bulk-single-crystal device is usually not compatible with the existing complementary metal–oxide semiconductor technology. To address the above-mentioned challenges associated with bulk samples, large-area highly crystalline 2D c-MOF films with controlled thickness are urgently required for practical electronics, which will allow sufficient contact with the electrodes and ensure high device stability as well as adequate charge transport.^[6] Thus far, a great effort has been dedicated to the establishment of reliable synthetic methods toward the synthesis of large-area 2D

J. Liu, Y. Chen, X. Feng, R. Dong
Center for Advancing Electronics Dresden (CFAED) & Faculty of Chemistry
and Food Chemistry
Technische Universität Dresden
01062 Dresden, Germany
E-mail: xinliang.feng@tu-dresden.de, renhao.dong@tu-dresden.de

X. Feng
Max Planck Institute for Microstructure Physics
06120 Halle (Saale), Germany

R. Dong
Key Laboratory of Colloid and Interface Chemistry of the Ministry of
Education
School of Chemistry and Chemical Engineering
Shandong University
Jinan 250100, P. R. China

 The ORCID identification number(s) for the author(s) of this article can be found under <https://doi.org/10.1002/sstr.202100210>.

© 2022 The Authors. Small Structures published by Wiley-VCH GmbH. This is an open access article under the terms of the Creative Commons Attribution License, which permits use, distribution and reproduction in any medium, provided the original work is properly cited.

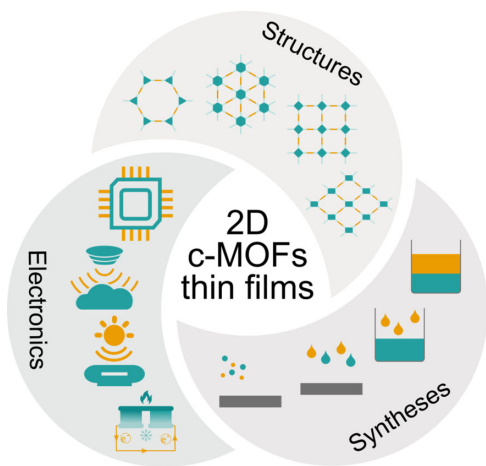
DOI: 10.1002/sstr.202100210

c-MOF films with high quality, which can be generally classified into two categories. One strategy is the exfoliation of bulk crystals and the subsequent assembly of the exfoliated nanosheets into films via solution processing, such as filtration and casting.^[18] This is a facile and high-yield approach to produce 2D c-MOF films with high utilization of active sites. Another strategy is the bottom-up synthesis of thin films through confined space,^[19] where the thickness of the thin film could reach from a few layers to monolayer.^[20] Benefiting from the development of film samples, various electronic devices with appealing performance could be realized, such as field-effect transistors (FETs),^[7,21–23] chemiresistive sensors,^[24–27] superconductors,^[28] photodetectors,^[10] and thermoelectrics.^[11,29]

In this review, we will summarize the state-of-the-art synthesis of 2D c-MOF thin films and functions for (opto-)electronics (**Scheme 1**). Powder 2D c-MOFs and their applications are not in the scope of this review; there are relevant reviews for various powder 2D c-MOFs.^[6,30,31] First, the molecular design of 2D c-MOFs is briefly introduced, and the fundamental understanding of structure–property relationship is presented. Second, we systematically introduce the synthesis methodologies toward the construction of 2D c-MOF thin films, including the exfoliation and reassembly (ERA) method, liquid-interface-assisted synthesis (LIAS) method, and chemical vapor deposition (CVD) method. In this section, we discuss the morphologies and crystallinity of representative 2D c-MOF film samples and provide an overview of the advantages and disadvantages of these synthetic methods. After that, we present the current achievements of the 2D c-MOF film-based (opto-)electronic applications, including the FETs, chemiresistive sensors, superconductors, and photodetectors. Finally, we present insight about current challenges and future development about 2D c-MOFs for (opto-)electronics, which is expected to be helpful for those interested in entering this exciting research area.

2. Molecular Design of 2D c-MOFs

2D c-MOFs are typical layered materials with strong in-plane conjugation and weak out-of-plane π - π stacking interaction that are highly analogous to graphene.^[30] They are generally



Scheme 1. Structures, syntheses, and electronics of 2D c-MOF thin films.

composed of ortho-substituted conjugated monomers with cross-linked transition metal ions. The first 2D c-MOF was reported by Yaghi et al. in 2012, where the obtained 2D layered porous extended frameworks comprised 2,3,6,7,10,11-hexahydroxytriphenylene (HHTP) and Cu atom.^[13] Currently, around 16 types of conjugated aromatic ligands have been designed and synthesized as construction building blocks, including 1,2,3,4,5,6-hexahydroxybenzene (HHB),^[32] 1,2,3,4,5,6-hexaaminobenzene (HAB),^[33] 1,2,3,4,5,6-benzenehexathiol (BHT or HTB),^[7] 1,2,3,4,5,6-benzenehexaselenol (HSeB),^[34] HHTP,^[13] 1,2,5,6,9,10-triphenylenehexathiol (THT or HHTP),^[20] 2,3,6,7,10,11-hexaaminotriphenylene (HATP),^[35] 2,3,6,7,10,11-triphenylenehexaselenol (HSeTP),^[36] 1,2,3,4,5,6,7,8,9,10,11,12-perthiolatedcoronene (PTC),^[12] 2,3,7,8,12,13-hexahydroxytetraazanaphthotetraphene (HHTT),^[14] 2,3,8,9,14,15-hexahydroxytrinaphthylene (HHTN),^[37] 2,3,7,8,12,13-hexahydroxytruxene (HHTX),^[38] metal 2,3,8,9,14,16-hexaaminohexaazatrinaphthylene (M₃HAHATN, M = Cu, Ni, and Co),^[39] metal 2,3,9,10,16,17,23,24-octahydroxyphthalocyanine (MPc(OH)₈, M = Fe, Ni, Cu, and Zn),^[40] metal 2,3,9,10,16,17,23,24-octaaminophthalocyanine (MPc(NH₂)₈, M = Cu),^[18] and metal 3,4,12,13,21,22,30,31-octahydroxynaphthalocyanine (MNPC(OH)₈, M = Ni).^[41] In addition, several substitution groups (labeled as X; X = H, A, T, Se, abbreviations of –OH, –NH₂, –SH, –SeH, respectively) and metal types (labeled as M) were employed as linkages, thereby leading to dozens of 2D c-MOFs with abundant physical and chemical characteristics.

Figure 1a,d,g presents three typical 2D network structures reported so far for 2D c-MOFs, including hexagonal lattice (**hxl**), honeycomb (**hcb**) lattice, and square lattice (**sql**), as well as the corresponding ligands and the as-formed 2D c-MOFs. The utilization of HTB or PTC ligands could result in **hxl**-type nonporous 2D coordination polymers owing to the D₆-symmetry, as shown in Figure 1b,c. But notably, HXB ligands (X = H, A, T, and Se) could also lead to 2D c-MOFs with **hcb** lattice, such as Cu-HHB,^[32] Ni-HTB,^[42] and M-HIB (M = Cu and Ni; HIB = hexaiminobenzene).^[33] While for the D₃-symmetric monomers (Figure 1e) based on triphenylene (HXTP, X = H, A, T, and Se)^[13,20,35,36] or tetraazanaphthotetraphene (HXTT, X = H)^[14] and D₄-symmetric monomers (Figure 1h) based on phthalocyanine (MPc(XH)₈, M = Fe, Ni, Cu, and Zn; X = O and NH)^[18,40] or naphthalocyanine (MNPC(XH)₈, M = Ni; X = O),^[41] the resulted 2D c-MOFs are generally formed as **hcb** (Figure 1h) and **sql** (Figure 1i) networks, respectively.

The molecular structures of 2D c-MOFs were highly correlated to their basic physical properties, such as bandgap and charge transport behavior.^[43] The 16 reported conjugated aromatic ligands and the corresponding 2D c-MOF samples are summarized in **Table 1**, including their molecular structures of lattice types, lattice parameters, and interlayer distances, as well as the electrical properties of electrical conductivities and mobilities. The nonporous 2D c-MOF samples with **hxl** lattice structure generally showed higher electrical conductivities compared to the ones with **hcb** networks. For example, Cu₃(HTB) and Cu₃(HSeB) could exhibit high electrical conductivities of 1580 and 110 S cm⁻¹,^[7,34] respectively, while Cu₃(HHB)₂ and Cu₃(HIB)₂ showed lower values of 7.3 × 10⁻⁸ and 13 S cm⁻¹,^[32,33] respectively. Such difference mainly originated from the varied topology networks and π - d hybridization in the 2D plane.

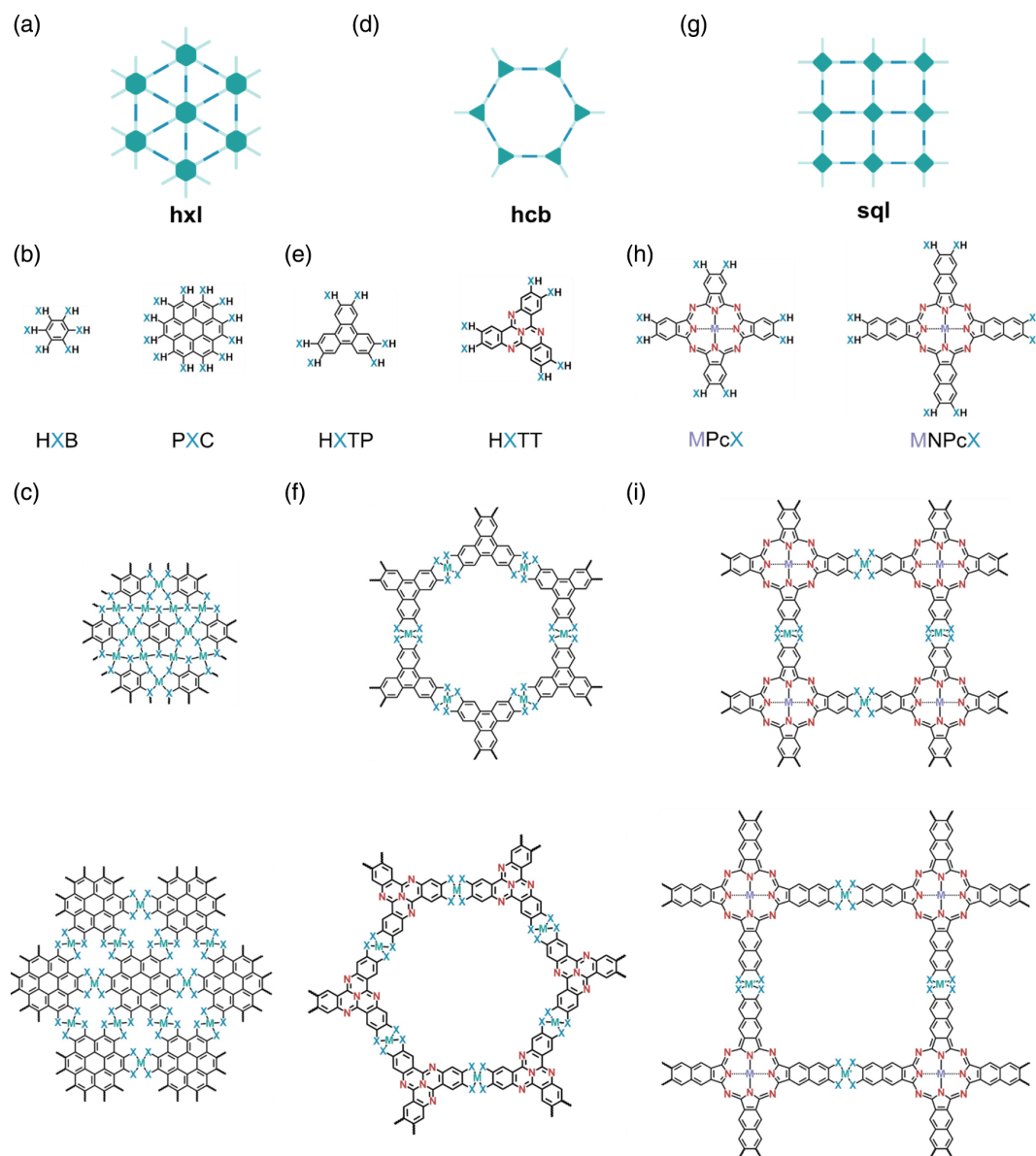


Figure 1. Schematic illustration of three typical lattice structures of 2D c-MOF networks, including a) hxl, d) hcb, and g) sql. Representative building blocks for constructing the corresponding 2D c-MOF networks, including b) benzene-based (HXB, X = H, A, T, and Se) and coronene-based (PXC, X = T) ligands for hxl lattice, e) triphenylene-based (HXTP, X = H, A, T, and Se) and tetraazaphthalotetraphene-based (HXTT, X = H) ligands for hcb lattice, h) phthalocyanine- (MPc(XH)₈, M = Fe, Ni, Cu, and Zn; X = O and NH) and naphthalocyanine-based (MNPc(XH)₈, M = Ni; X = O) ligands for sql lattice. The as-formed 2D c-MOFs, including c) M₃(HXB) (M = Cu and Ag) and M₃(PXC) (M = Fe, Ni, and Cu) with hxl lattice, f) M₃(HXTP)₂ (M = Fe, Ni, Cu, Co, and so on) and M₃(HXTN)₂ (M = Cu) with hcb lattice, and i) M'₂(MPcX₈) (M' = Fe, Ni, Cu, Co, and Zn) and M'₂(MNPcX₈) (M' = Ni, and Cu) with sql lattice.

In addition, varying the symmetrical functional groups (such as -OH, -NH₂, -SH) of the ligands and the transition metal nodes (M) will also lead to the coordination complexes with diverse π -*d* conjugation degrees, thereby greatly affecting their (opto-)electronic properties (such as bandgaps and in-plane charge transport properties).^[8,44–46] For instance, the 2D c-MOFs based on M-S coordination generally exhibited superior electrical conductivity to the samples based on M-O or M-N. For example, the Ni₃(HTB)₂ film showed a conductivity of

160 S cm⁻¹,^[47] while Ni₃(HIB)₂ and Ni₃(HHTP)₂ presented the conductivity of 8 S cm⁻¹ and 1.6 × 10⁻⁴ S cm⁻¹,^[33,48] respectively. The Fe₃(HTTP)₂ 2D c-MOF was demonstrated as an impressive active layer with a record charge mobility of ≈220 cm² V⁻¹ s⁻¹.^[9] In addition, the optoelectronic properties of 2D c-MOFs could also be tuned by the varying metal centers. It was calculated that the bandgaps of M₃(HTB) (M = Mg, Ca, Zn, Cd, Ge, and Sn) can be adjusted from 1.7 to 3.2 eV via employing diverse metal nodes.^[46] The single-layer Ni₃(HITP)₂

Table 1. Summary of the reported conjugated ligands and the corresponding 2D c-MOFs.

Ligands	2D c-MOFs	2D lattices	Lattice parameters	Interlayer distances	Electrical conductivities	Mobilities	References
HHB	Cu ₃ (HHB) ₂	hcb	$a = 1.31$ nm	$d = 0.296$ nm	7.3×10^{-8} S cm ⁻¹	N/A ^{a)}	Bao et al. ^[32]
HAB	Ni ₃ (HIB) ₂	hcb	$a = 1.35$ nm	$d = 0.33$ nm	8 S cm ⁻¹	N/A	Dincă et al. ^[33]
	Cu ₃ (HIB) ₂	hcb	$a = 1.35$ nm	$d = 0.33$ nm	13 S cm ⁻¹	N/A	Dincă et al. ^[33]
HTB	Cu ₃ (HTB)	hxl	$a = 0.845$ nm	$d = 0.338$ nm	1580 S cm ⁻¹	99 cm ² V ⁻¹ s ⁻¹ (Hole) 116 cm ² V ⁻¹ s ⁻¹ (Electron)	Zhu et al. ^[7]
HSeB	Cu ₃ (HSeB)	hxl	$a = 0.896$ nm	$d = 0.368$ nm	110 S cm ⁻¹	N/A	Zhu et al. ^[34]
HHTP	Ni ₃ (HHTP) ₂	hcb	$a = 2.19$ nm	$d = 0.33$ nm	N/A	N/A	Yaghi et al. ^[13]
	Co ₃ (HHTP) ₂	hcb	$a = 2.21$ nm	N/A	N/A	N/A	Yaghi et al. ^[13]
	Cu ₃ (HHTP) ₂	hcb	N/A	N/A	2.1×10^{-1} S cm ⁻¹	N/A	Yaghi et al. ^[13]
HTTP	Ni ₃ (HTTP) ₂	hcb	$a \approx 2$ nm	N/A	N/A	N/A	Dong et al. ^[20]
HATP	Ni ₃ (HITP) ₂	hcb	$a = 2.17$ nm	$d = 0.33$ nm	40 S cm ⁻¹	N/A	Dincă et al. ^[35]
HSeTP	Co ₃ (HSeTP) ₂	hcb	$a = 2.37$ nm	$d = 0.34$ nm	10^{-6} S cm ⁻¹	N/A	Zhu et al. ^[36]
PTC	Fe ₃ (PTC)	hxl	$a = 1.2$ nm	$d = 0.39$ nm	10 S cm ⁻¹	N/A	Dong et al. ^[12]
HHTT	Cu ₃ (HHTT) ₂	hcb	N/A	$d = 0.319$ nm	≈ 1 S cm ⁻¹	N/A	Dincă et al. ^[14]
HHTN	Cu ₃ (HHTN) ₂	hcb	$a = 2.94$ nm	$d = 0.329$ nm	9.55×10^{-10} S cm ⁻¹	N/A	Mirica et al. ^[37]
HHTX	Cu ₃ (HHTX) ₂	hcb	$a = 2.65$ nm	$d = 0.322$ nm	8.38×10^{-4} S cm ⁻¹	N/A	Zhang et al. ^[38]
Ni ₃ HAHATN	Ni ₃ (Ni ₃ HAHATN) ₂	hcb	$a = 2.95$ nm	$d = 0.343$ nm	2 S cm ⁻¹	N/A	Chen et al. ^[39]
FePc(OH) ₈	Fe ₂ FePcO ₈	sql	$a = 1.81$ nm	$d = 0.33$ nm	2×10^{-5} S cm ⁻¹	0.1 cm ² V ⁻¹ s ⁻¹ (Hall mobility)	Dong et al. ^[40]
CuPc(NH ₂) ₈	Ni ₂ CuPc(NH) ₈	sql	$a = 1.8$ nm	$d = 0.324$ nm	1×10^{-4} S cm ⁻¹	1.6 cm ² V ⁻¹ s ⁻¹ (Hall mobility)	Dong et al. ^[18]
NiNPc(OH) ₈	Ni ₂ NiNPcO ₈	sql	$a = 2.3$ nm	$d = 0.32$ nm	1.8×10^{-2} S cm ⁻¹	N/A	Mirica et al. ^[41]
	Cu ₂ NiNPcO ₈	sql	$a = 2.3$ nm	$d = 0.32$ nm	3.1×10^{-2} S cm ⁻¹	N/A	Mirica et al. ^[41]

^{a)}N/A: not applicable.

was predicted as an indirect semiconductor, while the single-layer Cu₃(HITP)₂ was metallic.^[8]

In addition to single-ligand and single-metal systems, multi-component 2D c-MOFs can also be achieved with fine tailored structures and compositions via the combination of multiple ligands or multiple metal nodes, further extending the library of 2D c-MOFs. For instance, our group reported triphenylene-based 2D c-MOFs with three different metal complexes via linking HTTP and HATP ligands together (**Figure 2a**), including metal bis(dithiolene) (MS₄), metal bis(diamine) (MN₄), and metal dithiolene-diamine (MS₂N₂, M = Co and Ni).^[49] The single-layer c-MOF nanosheets were synthesized at an air/water interface using HTTP and HATP as ligands, and the powder samples were synthesized by hydrothermal approach in a Teflon autoclave. Such 2D c-MOFs with abundant active sites can be utilized as model catalysts for the understanding of the activity origin of the catalytic reactions. In this respect, we applied the abovementioned 2D c-MOFs for electrocatalytic hydrogen evolution reaction, which demonstrated that the electrocatalytic activity of MS₂N₂ is higher than those of MN₄ and MS₄ complexes. Nishihara et al. reported another multicomponent 2D c-MOF based on bis(iminothiolato)nickel complex.^[50] As shown in **Figure 2b**, this 2D c-MOF was constructed via coordinating Ni²⁺ ions with 1,3,5-triaminobenzene-2,4,6-trithiol ligands. Thin-film samples were obtained at the dichloromethane/water

(DCM/water) interface and displayed an electrical conductivity of about 10⁻¹ S cm⁻¹ at room temperature. In the case of metal-node engineering, Dincă et al. reported the isostructural M¹_xM²_{3-x}(HITP)₂ (M¹M² = CuNi, CoNi, and CoCu; 0 ≤ x ≤ 1; HITP = 2,3,6,7,10,11-hexaiminotriphenylene) alloys via simultaneously introducing bimetals in an isolated HITP-based 2D c-MOFs.^[51] Continuous changes of the electrical conductivity from 0.024 to 55.4 S cm⁻¹ were realized associated with the bandgap narrowed by 400 meV via precisely altering the metal constituents in the binary 2D c-MOF alloys. In addition to varying the ligands and metal nodes, the recent advance has demonstrated that the interlayer transport pathway considerably contributes to the long-range charge transport in 2D c-MOF.^[15] Therefore, it is also an efficient strategy to tune the electrical properties through modifying the interlayer distance or adjusting the layer stacking model.

As is seen, the precision molecular design is highly demanded for the realization of structural control and property tuning of 2D c-MOFs, which is also in favor of in-depth understanding of the structure–property relationship and extending the applications to the electronic- and energy-related application areas. For more detailed structure–electronic property relationships of 2D c-MOFs, please refer to the recently published review articles.^[5,6] In the next sections, the discussion of synthesis and (opto-) electronic devices of 2D c-MOF thin films is focused.

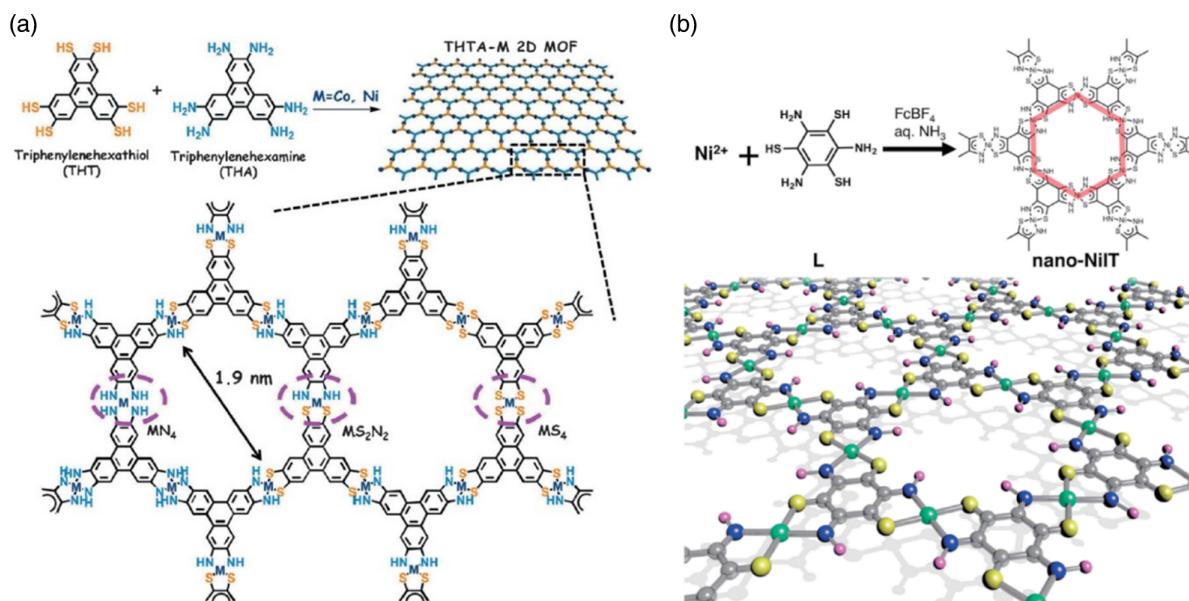


Figure 2. a) Schematic synthesis of multicomponent 2D c-MOFs based on metal dithiolene-diamine. Reproduced with permission.^[49] Copyright 2017, Wiley-VCH. b) Schematic illustration of multicomponent 2D c-MOF based on nickel bis(iminothiolato). Reproduced with permission.^[50] Copyright 2017, The Chemical Society of Japan.

3. Chemical Synthesis of 2D c-MOF Thin Films

Thus far, a great effort has been dedicated to the development of diverse chemical methods toward the synthesis of 2D c-MOF thin films. In this section, three synthetic approaches are majorly introduced by consideration of the state-of-the-art progress, including ERA method, LIAS method, and CVD growth method, and their advantages and limits are systematically discussed.

3.1. Exfoliation and Reassembly

Top-down exfoliation method generally refers to the delamination of the synthetic 2D c-MOF bulk crystals into nanosheets via introducing external mechanical forces. Thin-film samples can be subsequently reassembled by the nanosheets via further solution processing methods, such as filtration^[18] and casting.^[52] In this case, this strategy involves ERA steps.

Our group recently reported the mechanical exfoliation of phthalocyanine-based 2D c-MOF crystals into nanosheets via a NaCl-assisted ball milling approach.^[18] In a typical procedure, the bulk crystals were fabricated by a solvothermal process and the crystal size of the obtained $\text{Ni}_2[\text{CuPc}(\text{NH})_8]$ MOF was about 200 nm. Then, a ball milling process was performed with the assistance of NaCl, which could help reduce the shear forces and exfoliate the bulk sample into separated layers in a mild way, thereby increasing the yield without heavily reducing the crystal size, as shown in **Figure 3a**. The prepared 2D c-MOF layers exhibited an average thickness of about 7 nm and a lateral crystal size of about 160 nm, which was approximate to the original size of bulk samples. After exfoliation and removal of NaCl, the obtained samples could be uniformly dispersed in dimethylformamide (DMF) with a concentration of about 0.3 mg mL^{-1} , which was in favor of facile film processability via solution

processing. Centimeter-scale $\text{Ni}_2[\text{CuPc}(\text{NH})_8]$ -based film could be easily realized after filtration and integrated into electrical devices. The film sample exhibited a typical p-type charge transport behavior with an electrical conductivity of $10^{-4} \text{ S cm}^{-1}$ and mobility of $1.5 \text{ cm}^2 \text{ V}^{-1} \text{ s}^{-1}$. In this work, electrochemically exfoliated graphene nanosheets could also be dispersed into the c-MOF nanosheets solution, and thus a hybrid graphene/MOF thin film was fabricated via vacuum filtration. The side-view scanning electron microscope (SEM) images of samples after being transferred onto Si wafer showed a dense thin film with a thickness of about $6 \mu\text{m}$ (**Figure 3b**). Interdigital electrodes based on such hybrid film were fabricated via employing a homemade mask during the filtration, which were directly transferred onto a flexible polyimide substrate to generate a micro-supercapacitor (MSC) device with polyvinyl alcohol/LiCl gel as electrolyte. The as-constructed MSC exhibited the performance of high cycling stability (capacitance retention of 91.4% after 5000 cycles) and high areal capacitance (18.9 mF cm^{-2}), thus demonstrating the great potential of 2D c-MOF thin films by ERA in the fabrication of energy devices.

In addition to ball milling, sonication can also be utilized as the power source for top-down exfoliation. Our group also reported a surfactant-assisted sonication method for acquiring three kinds of ultrathin 2D c-MOF nanosheets with a high yield (>80%), where the obtained nanosheet samples were single crystalline with a large lateral size up to $0.65 \mu\text{m}^2$ and a thickness less than 5 nm.^[52] Take the synthesis of Cu-HHB 2D c-MOF nanosheets as one example (as shown in **Figure 3c**); copper acetate ($\text{Cu}(\text{OAc})_2$) salts and tetrahydroxy-1,4-quinone ligands were mixed in an aqueous solution of anionic surfactant sodium dodecyl sulfate (SDS). The surfactant molecules with negatively charged head groups could steadily adsorb on the surface of Cu-HHB via electrostatic interaction.^[53] During the hydrothermal

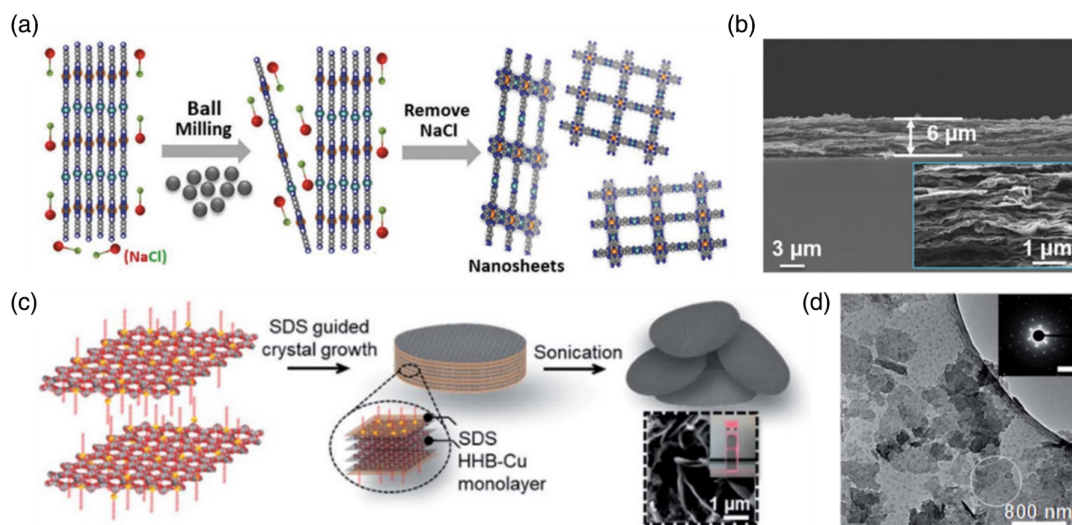


Figure 3. a) Schematic illustration of the NaCl-assisted ball milling exfoliation process of $\text{Ni}_2[\text{CuPc}(\text{NH})_8]$. b) Side-view SEM images of $\text{Ni}_2[\text{CuPc}(\text{NH})_8]$ -based hybrid thin film on Si wafer. a,b) Reproduced with permission.^[18] Copyright 2020, Wiley-VCH. c) Schematic illustration of the surfactant-assisted sonication process for exfoliating Cu-HHB c-MOF. d) TEM image of the exfoliated Cu-HHB samples. The scale bar of the inset is 1.85 nm^{-1} . c,d) Reproduced with permission.^[52] Copyright 2020, The Royal Society of Chemistry.

synthesis, the anchored SDS molecules could suppress the further stacking of Cu-HHB layers along the vertical direction, thereby favoring the 2D anisotropic growth behavior and the formation of ultrathin nanosheet samples. During the sonication-based exfoliation process, the adsorbed SDS molecules could also serve as a spacer to enlarge the interlayer distance and weaken the π - π stacking interaction of layered 2D c-MOFs, further expediting the sonication delamination. After exfoliation, the surfactant could prevent the reassembly or agglomeration of the delaminated layers and stabilize the final product. As a result, stable colloidal suspension (for at least 6 months) in the aqueous solution could be achieved, and the yield of nanosheets could reach 80–90%. The ultrathin and large-size nature of the exfoliated Cu-HHB nanosheets could be confirmed by the transmission electron microscopy (TEM) image (Figure 3d). The selected area electron diffraction (SAED) pattern indicated a hexagonal unit cell of the MOF with a parameter of 1.24 nm, which agreed well with the value of the Cu-HHB lattice. Thin-film samples were then prepared by casting the water-based slurry on a Cu foil, which served as the cathode for a Li-ion battery with LiPF_6 as the electrolyte and Li metal as the counter electrode. The as-prepared Li-ion battery showed a high rate capability (charge within 3 min, 81% , 1.0 A g^{-1} vs 0.1 A g^{-1}) and long-term cycling stability (capacity retention of 90% after 1000 cycles).

The ERA method is expected to be a facile and high-yield approach for producing thickness-tunable 2D c-MOF film samples. The acquired samples are generally featured with high utilization of active sites and possess great application potential in electrochemical and energy devices. However, the crystal size of the exfoliated nanosheets is restricted by the initial bulk crystals obtained from the hydro-/solvo-thermal methods, which generally generate powder samples with domain sizes less than a few micrometers. Moreover, the exfoliated samples also suffer from the drawbacks of poorly controlled morphologies, high defect

density, and nonuniform crystal sizes and thickness, thereby leading to reassembled films with degraded electrical performance. For constructing high-performance (opto-)electronic devices, the quality of the original bulk 2D c-MOFs as well as the fabricated thin-film samples needs to be further elevated.

3.2. Liquid-Interface-Assisted Synthesis Method

Bottom-up methods refer to the in situ controlled synthesis of 2D c-MOF films via directly linking ligand molecules and metal atoms. These methods are expected to offer much higher controllability during the synthesis process compared to the top-down approaches and lead to MOF films with high crystallinity, large size, and well-controlled thickness. In this section, as a recently developed bottom-up method, LIAS will be systematically introduced, including liquid–liquid (L/L) interface, gas–liquid (G/L) interface, and liquid–solid (L/S) interface. Such LIAS methods enabled to adjust the diffusion of monomers via tailoring the roughness of the liquid surface, thereby controlling the reaction. Moreover, the molecular orientation of monomers at the interface could also be regulated owing to the variable solvent/monomer and/or monomer/monomer interactions, which further alter their reactivity regarding the steric effect. All these features enable the liquid interfaces to serve as promising templates to modify the crystal growth and facilitate the thin-film formation of 2D c-MOFs.^[54]

3.2.1. Liquid–Liquid Interface

A L/L interface can be easily realized via overlaying an aqueous solution with an immiscible organic solution, as shown in Figure 4a. Generally, the organic ligands and metal salts are soluble in organic solvents and/or water. The L/L interfacial region offers a 2D confined space for the facile lateral mobility

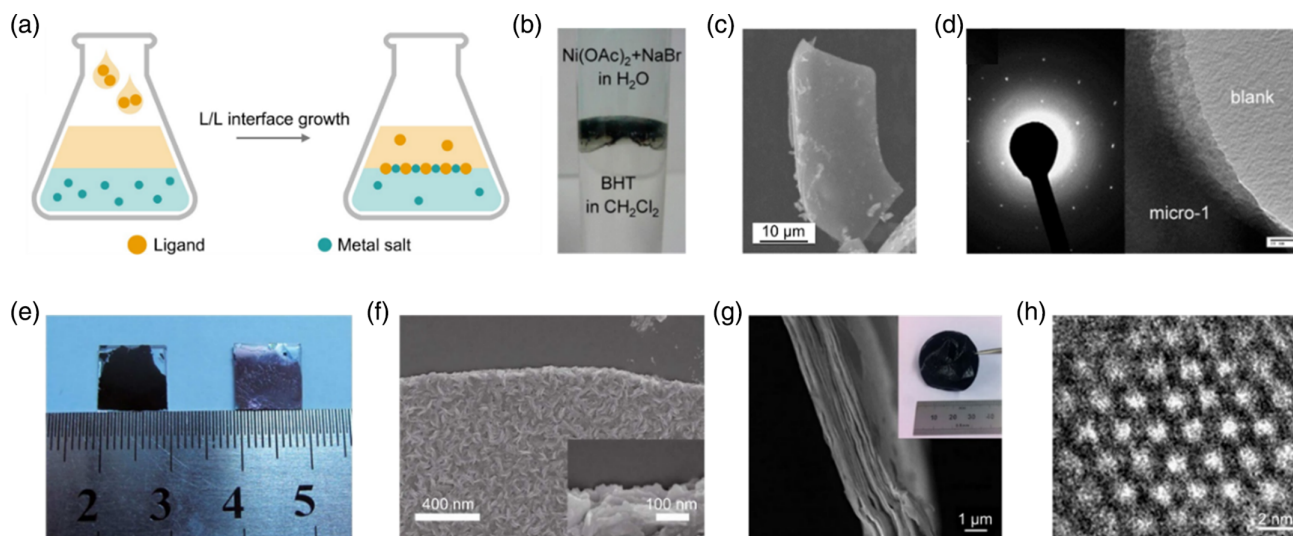


Figure 4. a) Schematic illustration of the L/L interfacial synthesis. b) Photograph of synthesis of $\text{Ni}_3(\text{HTB})_2$ films at the water–DCM interface. c) SEM image of the as-formed $\text{Ni}_3(\text{HTB})_2$ film. d) SAED pattern and TEM image of the $\text{Ni}_3(\text{HTB})_2$ film. a–d) Reproduced with permission.^[42] Copyright 2013, American Chemical Society. e) Photograph of the $\text{Cu}_3(\text{HTB})$ thin films transferred on glass substrates with downside surface (left) and upside surface (right) face up. f) Typical SEM image of the downside surface of synthesized sample and inset shows the edge of the film. e,f) Reproduced with permission.^[7] Copyright 2015, Springer Nature. g) SEM image of the synthesized $\text{Fe}_3(\text{HTTP})_2$ thin film in side view. h) HRTEM image of $\text{Fe}_3(\text{HTTP})_2$ with ordered hexagonal network structure. g,h) Reproduced with permission.^[9] Copyright 2018, Springer Nature.

of the monomers, which enables the growth of large-area continuous 2D structures. The liquid–liquid interfacial region offers a 2D confined space for the facile lateral mobility of the monomers, which enables the growth of large-area continuous 2D structures. In 2013, Nishihara et al. reported a representative work to synthesize 2D $\text{Ni}_3(\text{HTB})_2$ films with an **hcb** lattice structure at the L/L interface.^[42] DCM and water were employed as two immiscible liquid phases to dissolve HTB ligands and nickel acetate ($\text{Ni}(\text{OAc})_2$) salts, respectively. Figure 4b shows the photo of the reaction at the interface, which generated $\text{Ni}_3(\text{HTB})_2$ films with a thickness of a few micrometers and a lateral size of about 100 μm (Figure 4c). A hexagonal pattern could be observed by the SAED (Figure 4d), which indicated a typical hexagonal lattice of $\text{Ni}_3(\text{HTB})_2$. The TEM imaging showed a stairlike morphology of the edge of $\text{Ni}_3(\text{HTB})_2$ (marked as micro-1 in the image), which suggested a layered structure of the 2D c-MOF. In addition, the achieved $\text{Ni}_3(\text{HTB})_2$ film could present a high electrical conductivity up to 160 S cm^{-1} .^[47] To extend applicable 2D c-MOF systems of this L/L interfacial synthesis approach, the same group subsequently reported the synthesis of $\text{Pd}_3(\text{HTB})_2$ films at the water/DCM interface.^[55] To prevent the reduction of Pd^+ ions into Pd nanoparticles, $\text{K}_3[\text{Fe}(\text{CN})_6]$ was introduced into the aqueous phase as an additive, which facilitated the film formation of 2D c-MOFs. The synthetic film showed a low electrical conductivity of $10^{-7} \text{ S cm}^{-1}$, where the value could be drastically increased to 0.39 S cm^{-1} after the sample was treated by I_2 .

In addition to the 2D c-MOFs with **hcb** lattice structures, the samples with a nonporous **hxl** network structure could also be realized via L/L approaches, such as $\text{Cu}_3(\text{HTB})$. Zhu et al. reported the synthesis of $\text{Cu}_3(\text{HTB})$ thin films at the DCM/water interface, where HTB was dissolved in DCM bottom phase and

copper(II) nitrate ($\text{Cu}(\text{NO}_3)_2$) was dissolved in water top phase.^[7] The area of the resultant $\text{Cu}_3(\text{HTB})$ film was larger than 1 cm^2 (as shown in Figure 4e), and the thickness could be varied from 15 to 500 nm via controlling the reaction time. The optical image (left in Figure 4e) and the SEM image (Figure 4f) indicated a highly rough surface at the downside of the film facing the organic phase, while the upside toward the water phase exhibited a flat surface with fewer steps or cracks (right in Figure 4e). The difference is due to that the increased film thickness would weaken the interface-confining effect and then lead to the less-ordered crystal layers with a high-roughness surface. Grazing incident X-ray diffraction revealed that the synthesized $\text{Cu}_3(\text{HTB})$ films with 60 nm thickness preferred a face-on orientation, while the one with 200 nm thickness was highly heterogeneous without any layer orientation. The results demonstrated that the 2D c-MOF nanocrystals were randomly formed at the film surface near the L/L interface. Moreover, the thin film with a thickness of 400 nm exhibited an electrical conductivity value of 1580 S cm^{-1} . High electron and hole mobility values of 99 and $116 \text{ cm}^2 \text{ V}^{-1} \text{ s}^{-1}$ were also achieved by this ambipolar active material, respectively. In addition to the two typical coordination structures of **hcb** and **hxl**, 2D c-MOF thin films with an uncommon coordination structure, i.e., $\text{Ag}_5(\text{HTB})$, could also be synthesized at the L/L interface.^[56] The synthesis of this silver-based coordination polymer thin film was performed at the interface of toluene and water, which hosted HTB ligands and silver(I) nitrate (AgNO_3), respectively. The obtained samples showed an uncommon coordination structure owing to diverse coordination types of silver ions. The molecular structure was solved as a lamellar structure composed of inorganic 2D Ag–S networks and organic 1D Ag-dithiolene coordination polymers. A morphology difference between the two sides of the film was also observed,

where the water-contact side exhibited a flat surface, and the toluene-contact side was composed of needle-shaped nanocrystals. Moreover, the as-synthesized films featured a high electrical conductivity at room temperature, where the value could reach 250 S cm^{-1} .

Apart from the 2D c-MOFs based on HTB ligands, our group reported the L/L interfacial synthesis of HTTP-based 2D c-MOF thin films, i.e., $\text{Fe}_3(\text{HTTP})_2$ with an hcb network structure.^[9] Here, the aqueous phase hosted the HTTP ligand precursors and iron acetylacetonate ($\text{Fe}(\text{acac})_2$) was dissolved in the chloroform (CHCl_3) phase. Centimeter-sized 2D c-MOF films with thickness ranging from 20 nm to about $2 \mu\text{m}$ were realized at the $\text{CHCl}_3/\text{water}$ interface by varying reaction time and concentration of monomers (Figure 4g), and the crystal domain sizes ranged from tens to hundreds of nanometers. Both the high-resolution TEM (HRTEM) image (Figure 4h) and the SAED pattern indicated an ordered hexagonal network structure with a unit cell size of $\approx 1.97 \text{ nm}$. The X-ray diffraction (XRD) spectra suggested an AA stacking model with an interlayer distance of about 0.33 nm. A specific surface area of about $526 \text{ m}^2 \text{ g}^{-1}$ of the $\text{Fe}_3(\text{HTTP})$ thin films was calculated by measuring the nitrogen sorption isotherms. The time-resolved terahertz spectroscopy indicated a room-temperature mobility reaching as high as $220 \text{ cm}^2 \text{ V}^{-1} \text{ s}^{-1}$ of the synthesized films. A direct bandgap of the $\text{Fe}_3(\text{HTTP})_2$ was predicted by the density functional theory (DFT) calculations, where the infrared optical transmission measurements indicated an absorption onset of $\approx 250 \text{ meV}$. Subsequently, Marinescu et al. further reported the synthesis of Fe-HTTP at the L/L interface in 2019,^[57] where the HTTP ligand was treated with *N*-methyl-2-pyrrolidone and dissolved in ethyl acetate. The 2D c-MOF samples were synthesized with a thickness ranging from 84 to 410 nm at the ethyl acetate/water interface. With the abovementioned representative 2D c-MOF examples, highly crystalline thin films could be achieved at the L/L interface and were able to exhibit record electrical

conductivity (1580 S cm^{-1} for $\text{Cu}_3(\text{HTB})$) and charge mobility ($220 \text{ cm}^2 \text{ V}^{-1} \text{ s}^{-1}$ for $\text{Fe}_3(\text{HTTP})_2$). Such high crystallinity could be attributed to the 2D-space confinement and diffusion processes of reactants, which could lead to the pre-organization of ligands at the interface, slow down coordination reaction rates, and improve coordination reversibility, thereby improving the sample crystallinity. Of course, the unambiguous characterization of the pre-organization of the ligands at the L/L interface remains a challenge.

3.2.2. Gas-Liquid Interface

In addition to the L/L interfacial synthesis, the G/L interface strategy is also an efficient method for acquiring 2D c-MOF thin films (Figure 5a). Louie et al. reported G/L interfacial synthesis of several HAB-based 2D c-MOFs.^[22] Ethyl acetate solution containing metal acetylacetonate ($\text{M}(\text{acac})_2$, $\text{M} = \text{Ni}, \text{Cu}, \text{Co}$) salts was dropwise added to the surface of the HAB aqueous solution. After the evaporation of ethyl acetate, a continuous thin film was formed on the water surface with a thickness of about 10 nm. Xu et al. presented the synthesis of $\text{Ni}_3(\text{HITP})_2$ films at the air/water interface.^[21] After heating the aqueous solution containing HITP ligands, NiCl_2 , and trimethylamine, hydrophobic $\text{Ni}_3(\text{HITP})_2$ c-MOF nanoparticles were formed at the G/L interface. Owing to the interface-confining effect, the floated nanoparticles self-assembled into a continuous thin film on the smooth water surface, as shown in Figure 5b. The thickness of the synthesized sample could reach about 100 nm after a 3 min reaction, which featured an ultrasmooth surface and a compact film structure (Figure 5c). Hu et al. employed a vapor-induced conversion approach for synthesizing the $\text{Ni}_3(\text{HITP})_2$ films on the water surface with well-controlled thickness.^[58] As illustrated in Figure 5d, a bigger beaker filled with the aqueous solution of reactants was placed into a glass shield, in which a smaller beaker containing triethylamine (TEA) was also

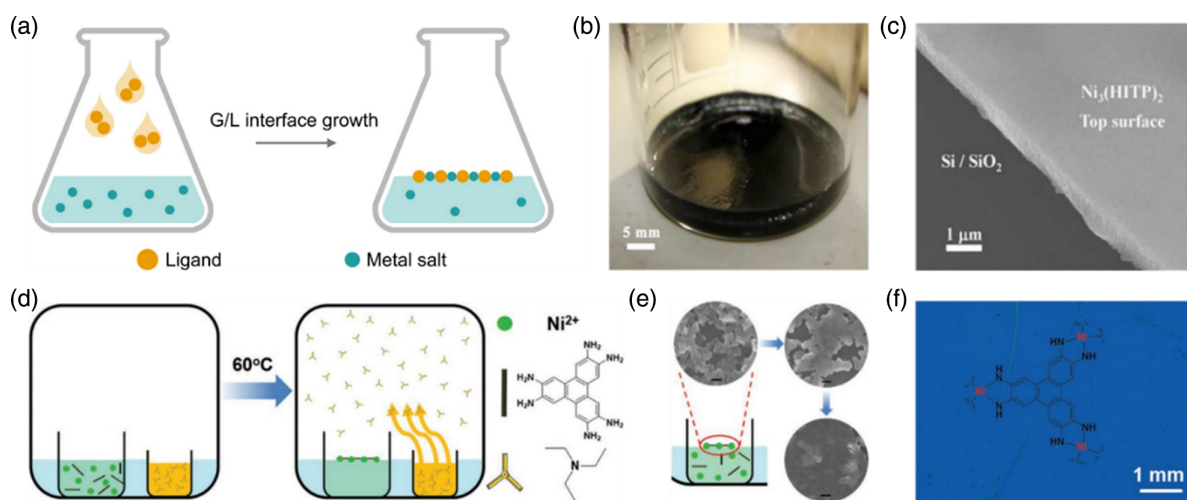


Figure 5. a) Schematic illustration of the G/L interfacial synthesis. b) Photograph of the $\text{Ni}_3(\text{HITP})_2$ thin film formed on the water surface. c) Typical SEM image of the synthesized $\text{Ni}_3(\text{HITP})_2$ thin film with an ultrasmooth surface and a compact film structure. a–c) Reproduced with permission.^[21] Copyright 2017, American Chemical Society. d) Schematic illustration of the vapor-induced conversion approach for synthesizing $\text{Ni}_3(\text{HITP})_2$ thin film at G/L interface. e) Sequential SEM images for the formation of the final film via assembling nanosized crystal spheres. f) Optical image of the obtained $\text{Ni}_3(\text{HITP})_2$ thin film. d–f) Reproduced with permission.^[58] Copyright 2019, Wiley-VCH.

placed. During heating, the TEA molecules were vaporized into the surrounding air and served as the alkaline source for triggering the formation of $\text{Ni}_3(\text{HITP})_2$. $\text{Ni}_3(\text{HITP})_2$ thin films comprising masses of nano-sized crystal spheres could be realized (Figure 5e), where the thickness of the final product (range from 7 to 92 nm) could be controlled by adjusting the concentration of the precursors in water (Figure 5f).

Recently, our group reported the synthesis of unique edge-on layer-oriented 2D c-MOF thin films at the G/L interface based on the $\text{MPc}(\text{OH})_8$ ($M = \text{Cu}$ and Fe) ligands.^[59] Such layer orientation of 2D c-MOFs on the water surface was originated from the edge-on self-assembly of the ligands, which was driven by the π - π interaction of ligand/ligand and hydrophobic interaction of ligand/water. In a typical synthesis procedure, the $\text{CuPc}(\text{OH})_8$ ligands were dissolved in a mixed solvent of CHCl_3 and DMF. The ligand solution was subsequently added onto the water surface and metal salts ($\text{Cu}(\text{OAc})_2$) were then added to the water phase after 30 min. $\text{Cu}_2\text{CuPcO}_8$ thin films with the edge-on structure were formed on the water surface after 18 h polymerization, which showed an average domain size of ≈ 600 nm and a thickness of ~ 20 nm. The electrical conductivity of the sample was measured to be about $5.6 \times 10^{-4} \text{ S cm}^{-1}$ at room temperature, and a Hall mobility of about $4.4 \text{ cm}^2 \text{ V}^{-1} \text{ s}^{-1}$ was also calculated. Benefiting from such an edge-on structure, the electrical conductivities through the in-plane (interlayer) and out-of-plane (intralayer) pathways could be investigated independently. The results indicated the anisotropic transport in this layered 2D c-MOFs, and the out-of-plane conductivity (about

$2 \times 10^{-3} \text{ S cm}^{-1}$) was much higher than the in-plane conductivity (about 10^{-6} – $10^{-5} \text{ S cm}^{-1}$). Furthermore, theoretical studies also supported that the interlayer charge transfer pathway dominated electrical transport in $\text{Cu}_2\text{CuPcO}_8$ thin films.

For acquiring the monolayer 2D c-MOFs, our group employed the Langmuir–Blodgett (LB)-assisted method for synthesizing monolayer $\text{Ni}_3(\text{HTTP})_2$ (HTTP, 2,3,6,7,10,11-triphenylenehexathiol) films at the air–water interface in 2015.^[20] As schemed in Figure 6a,^[19] the HTTP ligands (marked as M1) were first spread over the water surface in the LB trough via adding the precursor solution. After that, the surface pressure was increased to about 10 mN m^{-1} , which led to the assembly of ligand molecules and the formation of a dense monolayer. The solution of Ni salts (marked as M2) was then injected into the aqueous phase, and the Ni^{2+} ions were coordinated with the HTTP molecules to form 2D c-MOFs. A large-area and free-standing monolayer $\text{Ni}_3(\text{HTTP})_2$ film could be achieved at the air/water interface (Figure 6b). The sample could be easily transferred to the target substrates, including SiO_2/Si , Cu grid, or glassy carbon electrode for characterizations or applications. Figure 6c showed the typical SEM image of single-layer $\text{Ni}_3(\text{HTTP})_2$ film transferred on 300 nm SiO_2/Si wafer, and the atomic force microscope (AFM) measurement of the monolayer sheet suggested a thickness of about 0.7 nm, as shown in Figure 6d, thereby demonstrating the monolayer nature of the sample. For the sample transferred on the Cu grid, TEM measurements were carried out at cryogenic temperature to stabilize the monolayer $\text{Ni}_3(\text{HTTP})_2$ under the irradiation of a high-energy electron

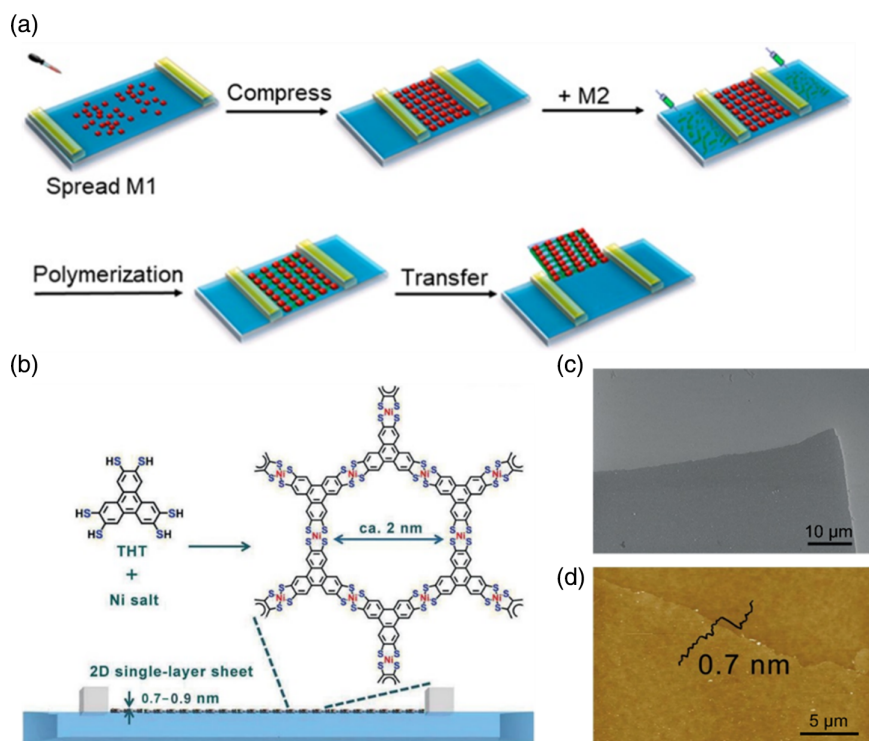


Figure 6. a) Schematic illustration of the LB-assisted G/L interfacial synthesis. Reproduced with permission.^[19] Copyright 2018, American Chemical Society. b) Schematic illustration of synthesizing monolayer $\text{Ni}_3(\text{HTTP})_2$ film via LB-assisted G/L method. c) SEM image of the monolayer $\text{Ni}_3(\text{HTTP})_2$ film. d) AFM image and the corresponding height profile of monolayer $\text{Ni}_3(\text{HTTP})_2$ film with a thickness of about 0.7 nm. b–d) Reproduced with permission.^[20] Copyright 2015, Wiley-VCH.

beam. SAED results indicated the typical hexagonal pattern of this ordered honeycomb network and a cell length of about 2 nm was calculated. Subsequently, Cao et al. reported the synthesis of monolayer and few-layer $\text{Co}_3(\text{HHTP})_2$ thin films based on the LB method and demonstrated the great potential of ultrathin 2D c-MOF layers in the energy devices.^[60]

3.2.3. Liquid–Solid Interface

For fabricating (opto-)electronics devices (e.g., FETs, sensors, superconductors, and photodetectors), 2D c-MOF samples synthesized at L/L or G/L interface were generally required to transfer onto the dielectric substrates (e.g., SiO_2/Si). However, the transfer process easily produced wrinkles or damaged the samples,^[61] thereby degrading the device performance. Compared to the L/L- and G/L-based methods, the L/S interfacial synthesis approaches could directly fabricate thin films on the target substrates and avoid the additional transfer, which was in favor of further device integration. Dincă et al. reported a facile L/S synthesis method via adding a solid substrate in the monomer aqueous solution (NiCl_2 , ammonia, and HATP ligands) during the reaction.^[35] $\text{Ni}_3(\text{HITP})_2$ films with a thickness of about 500 nm were formed on the quartz substrate. Xu et al. exhibited a spray layer-by-layer liquid-phase epitaxial method to directly

synthesize $\text{Cu}_3(\text{HHTP})_2$ films on the target substrate.^[27] Here, the substrates with $-\text{OH}$ functionalized surface were alternatively exposed to the ethanolic solutions of $\text{Cu}(\text{OAc})_2$ salts and HHTP ligands, as shown in **Figure 7a**. Face-on orientated 2D c-MOF films were prepared via cycling the spraying procedure, where each growth cycle could increase a thickness of 2 nm on average. Therefore, the thickness of the samples can be adjusted from 20 to 100 nm. The SEM images in **Figure 7b** indicated a continuous thin film synthesized after 40 growth cycles, which was formed by dense nanocrystals with a thickness of about 80 nm. The hexagonal structure with the lattice parameters of $a = b = 2.175$ nm was confirmed by the SAED pattern (**Figure 7c**). After that, Xu's group also reported the synthesis of $\text{Cu}_3(\text{HITP})_2$ films with the thickness ranging from 20 to 100 nm based on the spray layer-by-layer epitaxial method.^[62] Chen et al. reported a different layer-by-layer growth method via alternatively immersing the functionalized target substrates into the ethanol solutions of reactants (HHTP ligands and $\text{Cu}(\text{OAc})_2$) and ethanol.^[63] The thickness of the synthesized $\text{Cu}_3(\text{HHTP})_2$ films could also be controlled by adjusting the growth cycles. This method offered an “in situ” approach to directly assemble 2D c-MOF films on the electrodes, which was in favor of realizing a well-controlled organic/electrode interface with enhanced contact.

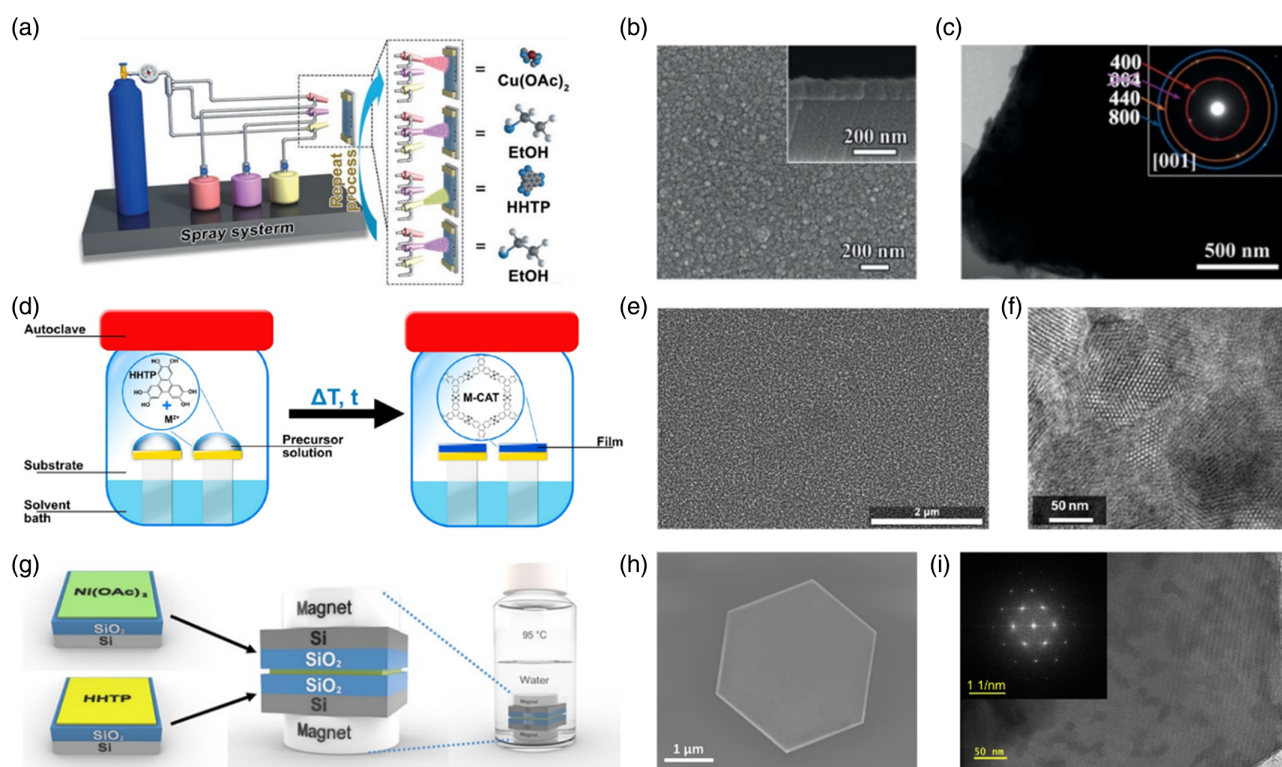


Figure 7. a) Schematic illustration of the spray layer-by-layer liquid-phase epitaxial method for synthesizing $\text{Cu}_3(\text{HHTP})_2$ films at the L/S interface. b) Top-view SEM image of acquired $\text{Cu}_3(\text{HHTP})_2$ film and inset showed the side-view SEM image. c) TEM image of the synthesized sample (inset image shows the corresponding SAED pattern). a–c) Reproduced with permission.^[27] Copyright 2017, Wiley-VCH. d) Schematic illustration of the vapor-assisted conversion method for directly synthesizing HHTP-based 2D c-MOF films on target substrates. e) SEM image and f) TEM image of the acquired $\text{Co}_9(\text{HHTP})_4$ thin films. d–f) Reproduced with permission.^[64] Copyright 2019, American Chemical Society. g) Schematic illustration of the solution-solid method to grow $\text{Ni}_3(\text{HITP})_2$ single crystals. h) SEM image and i) TEM image (inset shows the corresponding Fourier transform image) of the acquired $\text{Ni}_3(\text{HITP})_2$ single crystals. g–i) Reproduced with permission.^[67] Copyright 2021, American Chemical Society.

Medina et al. presented a vapor-assisted conversion method for directly synthesizing HHTP-based 2D c-MOF films on target substrates.^[64] As illustrated in Figure 7d, a solvent bath composed of water and 1-propanol was placed in a reaction vessel, which served as the vapor source during heating. The substrates placed inside were supported by elevated flat platforms to prevent direct contact with the solvent bath. The HHTP ligands and metal ions (Ni^{2+} , Co^{2+} , or Cu^{2+}) were dissolved in a mixture of solvent of water and 1-propanol, and then spread onto the substrate surfaces with full coverage. Here, 1-propanol was employed as an adjuster for achieving 2D c-MOF thin films with large domain sizes. $\text{Cu}_3(\text{HHTP})_2$, $\text{Ni}_9(\text{HHTP})_4$, and $\text{Co}_9(\text{HHTP})_4$ with domain sizes of about 10, 2, and 4 μm , respectively, were realized after heating the reaction vessel. The SEM image suggested that the 2D c-MOF thin films were formed by packed pillared crystals with thicknesses of about 200 nm and free of crack over a large area (Figure 7e). The presence of preferential orientation of the films was revealed by the grazing-incidence wide-angle X-ray scattering patterns. The results suggested that the stacking reflections of the crystals were aligned orthogonally to the substrate surface. The TEM image in Figure 7f confirmed the typical hexagonal network structures and revealed the high-crystalline feature of the vapor-assisted conversion samples. Liu et al. proposed an electrochemical synthesis approach to acquire several Cu-based 2D c-MOF films.^[65] In a typical reaction, HHTP ligands were injected into the deionized water accompanied by ammonia for deprotonation. Two pieces of Cu foil were submerged into the prepared aqueous solution and separately attached to the two terminals of a direct-current power supply to construct an electrochemical reaction cell. After providing a suitable voltage, Cu^{2+} ions would be released from the anode Cu foil and coordinated with HHTP anions for forming $\text{Cu}_3(\text{HHTP})_2$ thin films on the cathode Cu foil. Here, the applied voltage could directly control the electrolysis of Cu, thereby regulating the thickness and morphology of the as-synthesized 2D c-MOF samples. The AFM measurements of the obtained continuous film revealed a maximum thickness of about 60 nm and an average surface roughness of about 1.6 nm. The same group also developed a face-to-face confinement growth method to synthesize 2D c-MOF films on solid substrates based on the capillary phenomenon.^[66] Before reaction, two dielectric substrates functionalized by $-\text{OH}$ groups were stacked face to face for constructing a confined interspace. The hydrophilic substrate surfaces were employed to generate the capillary effect, which could pump the reactant solution into the interspace and promote the coordination reaction. For reducing the nucleation density on the surface, a trace amount of solution containing low-concentration metal ions (Cu^{2+} , Co^{2+} , and Ni^{2+}) was injected into the confined area, where the ions would attach to the functionalized surface as preliminary nucleation sites. After that, a small amount of low-concentration ligand (HHTP) solution was cyclically derived into the interspace. The ligand monomers were subsequently coordinated with metal ions to form HHTP-based 2D c-MOF films at the dielectric substrate surface.

The abovementioned methods generally lead to polycrystalline 2D c-MOF films with widespread grain boundaries, which will greatly influence their intrinsic properties. In contrast, single-crystal samples could ensure the reliable analysis of their

intrinsic characteristics, which can lead to an authentic structure–property relationship and promote the further developments of 2D c-MOFs.^[14] For acquiring sizeable single-crystal 2D c-MOFs, Baldo et al. proposed a solution-solid method to grow single crystals with lateral sizes larger than 10 μm at the L/S interface.^[67] For promoting the coordination rates between ligands and metals rather than improving the π – π stacking rates, high concentrations of the precursors and high reaction temperature were maintained during the synthesis process. As schemed by Figure 7g, the HHTP ligands were deposited on the SiO_2/Si substrate via thermal evaporation, and the metal salt precursors, $\text{Ni}(\text{OAc})_2$, were deposited on another substrate as a thin film via drop-casting. The two substrates were placed face to face with the reactant films tightly contact. A confined interspace between the two substrates was realized via employing two coin magnets, and the entirety was immersed into water with heating at 95 °C. Here, the HHTP molecules were attached to the silicon substrate surface via hydrogen bonding interaction, which can align these reactant molecules to define the growth direction of $\text{Ni}_3(\text{HHTP})_2$ product at the substrate surface. Only a trace amount of solvent was permitted to inject into the confined reaction volume during the synthesis, which enabled to remain the solid phase of the HHTP thin film. Thus, the 2D c-MOF could nucleate on the solid HHTP film with aligned molecules and rapidly grow into large crystals in the environment of high-concentration reactants. Moreover, the entire configuration could also confine the enlargement of the samples in the vertical direction, thereby triggering the 2D anisotropic growth behavior and leading to 2D c-MOF single crystals with large sizes. The SEM image of a typical $\text{Ni}_3(\text{HHTP})_2$ single crystal is shown in Figure 7h, which suggests an ideal geometrical crystal with hexagonal morphology and sharp edges. A thickness of about 600 nm was indicated by AFM. The crystallinity of the sample was characterized by the TEM measurements, and the fast Fourier transform (FFT) of the HRTEM image showed only one set of patterns, thereby confirming the single-crystallinity nature of the hexagonal crystals.

As listed in Table 2, the developed LIAS methods lead to various 2D c-MOF films with large sizes, which allowed the integration of numerous functional devices with the synthesized samples as core building blocks. We could find out that the employment of the G/L interface generally led to thin films with ultrathin thickness, even allowing the formation of monolayer samples.^[20,60] The 2D c-MOF samples synthesized via L/L interface generally exhibited high quality, which enabled us to realize recorded electrical conductivity (1580 S cm^{-1} of $\text{Cu}_3(\text{HTB})$)^[7] and charge mobility ($220 \text{ cm}^2 \text{ V}^{-1} \text{ s}^{-1}$ of $\text{Fe}_3(\text{HHTP})_2$).^[9] Different from the L/L and G/L methods, the L/S interfacial synthesis dominated the superiorities of high compatibility toward (opto-)electronic devices integration and high controllability of film thickness.^[27,63,66] However, the extension of these strategies is rather limited by the reaction environment, as only the precursors with adequate solubility in organic solvents or water can be selected as reactants. The presence of a solvent will also generate concerns over the issues related to chemical contamination and contact corrosion, which are unfavorable for the microelectronic integration processes.^[68] Moreover, these strategies generally result in polycrystalline 2D c-MOF thin films formed by nanometer-scale domains. More efforts on effectively controlling

Table 2. Summary of the 2D c-MOF thin films synthesized by LIAS methods.

LIAS methods ^{a)}	Thin films	Ligands	Metal salts	Interfaces	Thickness	Electrical conductivities	References	
L/L	Ni ₃ (HTB) ₂	HTB	Cu(OAc) ₂	DCM/water	1–2 μm	160 S cm ⁻¹	Nishihara et al. ^[42]	
	Pd ₃ (HTB) ₂	HTB	K ₂ PdCl ₄	DCM/water	2–3 nm	10 ⁻⁷ S cm ⁻¹	Nishihara et al. ^[55]	
						0.39 S cm ⁻¹ (after treated by I ₂)		
	Cu ₃ (HTB)	HTB	Cu(NO ₃) ₂	DCM/water	15–500 nm	1580 S cm ⁻¹ (400 nm-thick sample)	Zhu et al. ^[17]	
	Ag ₅ (HTB)	HTB	AgNO ₃	Toluene/water	N/A ^{a)}	250 S cm ⁻¹	Zhu et al. ^[56]	
	Fe ₃ (HHTTP) ₂	HHTTP	Fe(acac) ₂	Water/CHCl ₃	20–2000 nm	3.4 × 10 ⁻² S cm ⁻¹	Dong et al. ^[9]	
G/L	Fe ₃ (HHTTP) ₂	HHTTP	FeCl ₂	Ethyl acetate/water	84–410 nm	0.2 S cm ⁻¹ (275 nm thick sample)	Marinescu et al. ^[57]	
	Ni ₃ (HIB) ₂	HAB	Ni(acac) ₂	Air/water	≈10 nm	N/A	Louie et al. ^[22]	
	Cu ₃ (HIB) ₂	HAB	Cu(acac) ₂	Air/water	≈11 nm	N/A	Louie et al. ^[22]	
	Co ₃ (HIB) ₂	HAB	Co(acac) ₂	Air/water	≈13 nm	N/A	Louie et al. ^[22]	
	Ni ₃ (HITP) ₂	HATP	NiCl ₂	Air/water	≈100 nm	40 S cm ⁻¹	Xu et al. ^[21]	
	Ni ₃ (HITP) ₂	HATP	NiCl ₂	Air/water	7–92 nm	0.85 S m ⁻¹ (7 nm thick sample)	Hu et al. ^[58]	
						2.23 S m ⁻¹ (40 nm thick sample)		
						22.83 S m ⁻¹ (92 nm thick sample)		
	Cu ₂ CuPcO ₈	CuPc(OH) ₈	Cu(OAc) ₂	Air/water	≈20 nm	2 × 10 ⁻³ S cm ⁻¹ (out of plane) 10 ⁻⁶ –10 ⁻⁵ S cm ⁻¹ (in plane)	Dong et al. ^[59]	
	Cu ₂ FePcO ₈	FePc(OH) ₈	Cu(OAc) ₂	Air/water	≈30 nm	N/A	Dong et al. ^[59]	
	Ni ₃ (HHTTP) ₂	HHTTP	Ni(NO ₃) ₂	Air/water	≈0.7 nm (monolayer)	N/A	Dong et al. ^[20]	
	Co ₃ (HHTTP) ₂	HHTTP	Co(OAc) ₂	Air/water	≈0.7 nm (monolayer) ≈2.85 nm (four-layer)	N/A	Cao et al. ^[60]	
	L/S	Ni ₃ (HITP) ₂	HATP	NiCl ₂	Water/quartz	≈500 nm	40 S·cm ⁻¹	Dincă et al. ^[35]
		Cu ₃ (HHTTP) ₂	HHTTP	Cu(OAc) ₂	Ethanol/Si or SiO ₂ or quartz or sapphire	20–100 nm	0.02 S cm ⁻¹ (80 nm thick sample)	Xu et al. ^[27]
		Cu ₃ (HITP) ₂	HATP	Cu(OAc) ₂	Ethanol/Si	20–100 nm	N/A	Xu et al. ^[62]
Cu ₃ (HHTTP) ₂		HHTTP	Cu(OAc) ₂	Ethanol/quartz	30–100 nm	0.29 S cm ⁻¹ (100 nm thick sample)	Chen et al. ^[63]	
Cu ₃ (HHTTP) ₂		HHTTP	Cu(C ₅ H ₄ F ₃ O ₂) ₂	Water and 1-propanol/Au or glass	≈2 μm	N/A	Medina et al. ^[64]	
Ni ₉ (HHTTP) ₄		HHTTP	Ni(OAc) ₂	Water and 1-propanol/Au or glass	≈200 nm	1.1 × 10 ⁻³ S cm ⁻¹	Medina et al. ^[64]	
Co ₉ (HHTTP) ₄		HHTTP	Co(OAc) ₂	Water and 1-propanol/Au or glass	≈200 nm	3.3 × 10 ⁻³ S cm ⁻¹	Medina et al. ^[64]	
Cu ₃ (HHTTP) ₂		HHTTP	Cu foil	Water and ethanol/Cu	4.13–60 nm	0.087 S cm ⁻¹ (20 nm thick sample)	Liu et al. ^[65]	
Cu ₃ (HHTTP) ₂		HHTTP	CuSO ₄	Water/quartz or SiO ₂ or sapphire	11–83 nm	3.3 mS cm ⁻¹	Liu et al. ^[66]	
Co ₃ (HHTTP) ₂		HHTTP	CoCl ₂	Water/quartz or SiO ₂ or sapphire	9–78 nm	2.8 mS cm ⁻¹	Liu et al. ^[66]	
Ni ₃ (HHTTP) ₂		HHTTP	NiCl ₂	Water/quartz or SiO ₂ or sapphire	10–85 nm	5.2 mS cm ⁻¹	Liu et al. ^[66]	
Ni ₃ (HHTTP) ₂		HHTTP	Ni(OAc) ₂	Water/SiO ₂	≈600 nm	2 S cm ⁻¹	Baldo et al. ^[67]	

^{a)}N/A: not applicable.

the orientation of the domains are still urgently required for improving the sample quality.

3.3. CVD Synthesis

CVD growth method, which has already proved its superiorities in the controllable growth of 2D inorganic crystals,^[69–72] is deemed as a feasible approach for acquiring desired MOF samples.^[68,73] Taking advantage of its superior controllability in the crystal growth process, several recent advances were proposed for acquiring 2D c-MOF samples.^[74,75]

Very recently, Liu et al. proposed the “in situ” growth of $\text{Cu}_3(\text{HHTP})_2$ 2D c-MOF samples based on a dual-zone heating CVD method.^[75] For a typical growth process, HHTP powders and cleaned Cu foil were employed as the reactants, which were placed on two different heating zones for maintaining different heating temperatures. As schemed by **Figure 8a**, organic ligands were heated to about 325 °C, while the Cu foil was maintained at 100 °C. The employed temperature setup could overcome the problem caused by the temperature distinction between the sublimation of HHTP precursors and decomposition of formed $\text{Cu}_3(\text{HHTP})_2$. During the growth, oxygenated water ($\text{O-H}_2\text{O}$) was injected into the reaction area with Ar as the carrier gas, which was regarded as the key additive for forming crystalline $\text{Cu}_3(\text{HHTP})_2$ samples. The authors suggested that O_2 could trigger the reversible interconversion of HHTP molecules into the forms of catecholates, semiquinone, and quinone. The strong oxidation tendency of quinone enabled the ionization of Cu atoms into Cu^{2+} ions so that the metal ions could coordinate with the deprotonated HHTP to form $\text{Cu}_3(\text{HHTP})_2$ seeds. In addition,

H_2O was believed to be the key to facilitating the crystallization of the final product.^[68] The SEM image in **Figure 8b** indicated that the synthesized $\text{Cu}_3(\text{HHTP})_2$ sample on the Cu foil was formed by dense-oriented nanowires. The SAED pattern of the single nanowire showed only one set of diffraction points (**Figure 8c**), which revealed the formation of the single-crystalline nanowires. Regarding that an additional transferring process was required for samples grown on metal substrates, directly growing 2D c-MOF thin films on insulation substrates would be much beneficial for device integration. Therefore, Whittaker-Brooks et al. investigated the CVD growth of Cu-HTB thin films on glass substrates via two synthesis routes, i.e., vapor–vapor interfacial CVD growth and solid–vapor interfacial CVD growth.^[74] As observed in **Figure 8d**, for the vapor–vapor interfacial growth, the organic precursors (i.e., HTB ligands) and metal precursors (i.e., $\text{Cu}(\text{acac})_2$) were put into two ceramic containers, which were separately placed in two heating zones of CVD furnace. The organic linkers were placed upstream and the metal salts were placed downstream, while the glass substrates were placed at the center of the dual-zone furnace. During heating, both precursors were sublimed into the vapor phase and diffused on the substrate surface for realizing polymerization. For solid–vapor interfacial growth, the setup of HTB ligands remained the same, while the metal precursors were deposited on the glass substrate via spin-coating a copper sulfate thin film. In this case, the coordination reaction of HTB and Cu^{2+} took place on the substrate surface, and the thickness of the as-grown 2D c-MOF thin films could be directly controlled by the thickness of spin-coated metal precursors and the growth durations. Both growth routes could yield Cu-HTB as continuous films overall substrate surface, but with obviously different morphologies and domain sizes. The

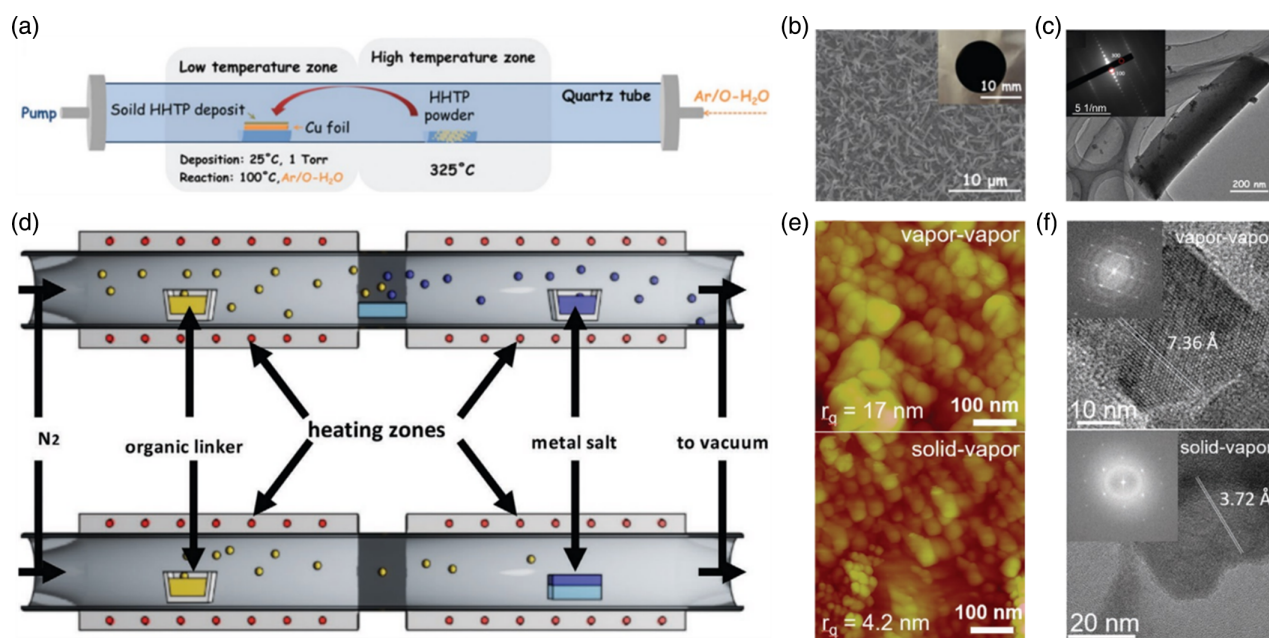


Figure 8. a) Schematic illustration of the CVD setup for “in situ” growth of $\text{Cu}_3(\text{HHTP})_2$ film on Cu foil. b) SEM image (inset shows the photograph of the resultant film sample) and c) TEM image (inset shows the corresponding SAED pattern) of the acquired $\text{Cu}_3(\text{HHTP})_2$ samples. a–c) Reproduced with permission.^[75] Copyright 2020, The Royal Society of Chemistry. d) Schematic illustration of the CVD setup for growing Cu-HTB thin films via vapor–vapor interfacial and solid–vapor interfacial synthesis routes. e) AFM images and f) TEM images (insets show the corresponding SAED patterns) of the acquired Cu-HTB thin films. d–f) Reproduced with permission.^[74] Copyright 2021, Wiley-VCH.

AFM results of two samples (Figure 8e) indicated that the domain sizes of vapor–vapor sample and solid–vapor sample varied from 60 to 100 nm and from 25 to 50 nm, respectively. In addition, a surface roughness of about 17 nm was measured from the vapor–vapor sample, while a value of about 4.2 nm was assigned to the solid–vapor sample with a much smoother surface. TEM measurements were also carried out to probe the lattice structure and stacking modes of the samples. The HRTEM images and corresponding FFT patterns suggested a remarkable difference in the interspace distances of two samples synthesized from different routes (Figure 8f). The results indicated a nonslipped AA stacking configuration of the vapor–vapor Cu-HTB and a slipped AB stacking mode of the solid–vapor sample. All these outcomes revealed that the phases of the precursors played an important role in the CVD growth of Cu-HTB c-MOFs. Although the currently reported 2D c-MOF film samples possess a large number of defects originating from the particle/phase boundaries and the low control of the coordination reaction progress, these preliminary works demonstrated the feasibility of the CVD approach toward the construction of 2D c-MOF thin film samples. In addition, it should be noted that the organic ligands or the MOF films could be carbonized after heating at high temperatures,^[76] which would lead to the limitations of CVD methods in terms of employing suitable reactants and growth temperatures. However, several rational strategies could be employed to avoid the ligands and MOFs from decomposition or carbonization during growth, such as employing high-vapor-pressure precursors, introducing vacuum environments, and pre-depositing reactants.^[68,74,75] All these strategies could enable the growth procedure to perform at a lower temperature, thereby extending the applicable MOF systems for CVD synthesis.

In addition to the large-area CVD synthesis, several vapor-phase growth works were proposed for forming single-layer 2D c-MOF domains with highly ordered orientations on monocrystalline metal surfaces. Generally, the growth processes were performed in the ultrahigh vacuum chamber based on the scanning tunneling microscope (STM).^[77–80] For example, Lackinger et al. investigated the formation of metal–organic networks via annealing the organic ligands on the metal surface in the STM chamber.^[77] A metal–organic cluster constituted by Cu₃ linked with three organic molecules could be identified. Ni₃(HITP)₂ frameworks with limited repeating units were also formed after adding Ni element on Cu surface. Apart from the 2D c-MOFs with common lattice structures, metal–organic networks with novel coordination structures could also be observed by STM. Fuchs et al. synthesized several HTB-based 2D c-MOFs with uncommon network structures on metal surfaces and analyzed them by STM.^[78] The deprotonation of HTB molecules was realized by elevating the surface temperature and then triggering the coordination reaction between metal atoms. Several frameworks including Ag₃(HTB) on Ag(111) surface, and Cu₆(HTB) and Cu₈(HTB) on Cu(111) surface were observed. These results offered the precise analysis of the molecular arrangements of the synthesized samples and also discovered several 2D c-MOF crystals with unconventional lattice structures. These results offered the precise analysis of the molecular arrangements on the solid substrates and also demonstrated unconventional lattice structures of 2D c-MOFs.

However, the synthesis via STM suffered from drawbacks of limited crystal size and rigorous growth environment. In addition, it is also complicated to transfer the MOF film samples from metal surfaces for further characterization and device integration.

In summary, ERA methods were advantageous for high yielding. The synthesized 2D c-MOF thin films were featured with high utilization of active sites, which generally exhibited great application potential in electrochemical and energy devices. However, the samples were rather limited by small crystalline domain sizes, high defect density and poorly controlled thicknesses, thereby leading to degraded electrical performance and greatly restricting their further developments in (opto-)electronic applications. In contrast, the bottom-up LIAS and CVD methods enabled the acquisition of various 2D c-MOF films with enlarged sizes and optimized crystallinity, which were favorable for the integration of numerous functional devices. Herein, the G/L interfacial synthesis allowed the formation of 2D c-MOFs with ultrathin thickness or even monolayer thickness, while the L/L interfacial synthesis exhibited great potential to obtain 2D c-MOF thin films with high crystallinity. Different from the L/L and G/L methods, the L/S methods demonstrated the superiorities of high compatibility toward (opto-)electronic devices integration and high controllability of film thickness due to the utilization of various solid substrates. However, the further developments of these strategies were rather limited due to the solution environment, which required adequate solubility of the precursors, and also generated concerns related to chemical contamination and contact corrosion. Moreover, the currently reported 2D c-MOF thin films by LIAS method were generally polycrystalline comprising nanometer-scale domains. The highly heterogeneous feature severely restricted the high device performance and the further understanding of structure–property relationships. Owing to the high controllability in the elementary crystal growth processes, the CVD method was regarded as a highly appealing approach toward highly crystalline or single-crystalline 2D c-MOFs, where the synthesis feasibility was demonstrated very recently. Regarding the possible thermal damage of organic ligands and MOFs at high heating temperatures, several rational strategies could be adapted to enable the growth procedure to perform at a lower temperature, thereby extending the applicable MOF systems for CVD synthesis.

4. Electronic and Optoelectronic Devices Based on 2D c-MOF Thin Films

Owing to their intrinsic high electrical conductivity combined with plentiful unique characteristics such as specific surface area, defined pore sizes and active sites, adjustable electronic structures, and high structural designability, 2D c-MOFs have exhibited the potential for electronic and optoelectronic devices. The consequence of the successful synthesis of film samples has further offered 2D c-MOF the superiority of facile processing and integration, thus enabling them as the active layers for realizing unique and high-performance (opto-)electronic devices, such as FETs,^[7,21–23] chemiresistive sensors,^[24–27,41,81–83] superconductors,^[28,84] photodetectors,^[10] and thermoelectrics.^[11,29]

4.1. FETs

FET is one of the key electronic components in the electronics industry, especially in integrated circuits. It is usually constructed based on a three-terminal structure, which can adjust the current flow via applying an additional electric field. Here, the employed active materials are expected to be semiconducting and compatible with device processing technology. 2D c-MOF thin films with tailorable electronic structures and high integration ability were introduced to confirm their application potential. In addition, FET measurement was also a general approach to efficiently investigate the electronic characteristics of 2D c-MOFs, such as the charge transport behavior and the charge mobility.

In 2015, Zhu et al. reported the bottom-gate FET devices based on the nonporous $\text{Cu}_3(\text{HTB})$ thin films and investigated the transport properties of this 2D c-MOF.^[7] The employed $\text{Cu}_3(\text{HTB})$ thin film was synthesized by the L/L interfacial approach, which showed an obvious difference in the surface roughness between its downside and upside surfaces. To ensure the connection of the insulated layer and electrodes with the smoother surface, a FET device with a bottom-contact configuration was constructed, as shown in **Figure 9a**. An ambipolar transport behavior of the 2D c-MOFs could be observed from the typical transfer curves of I_{ds} (drain-source current) versus V_{gs}

(gate-source voltage). The field-effect mobilities of $99 \text{ cm}^2 \text{ V}^{-1} \text{ s}^{-1}$, assigned to hole mobility (Figure 9b), and $116 \text{ cm}^2 \text{ V}^{-1} \text{ s}^{-1}$, assigned to electron mobility (Figure 9c), were extracted from the output curves, which confirmed a balanced ambipolar transport behavior of $\text{Cu}_3(\text{HTB})$. In addition, a low on/off ratio of about 10 of the device was also calculated, which stemmed from the metallic feature of $\text{Cu}_3(\text{HTB})$. Subsequently, Louie et al. investigated the bottom-gate FETs based on Ni-HAB c-MOFs.^[22] The fabricated devices with both top-contact and bottom-contact geometries showed similar resistance, and their transfer curves suggested a slight modulation of the conductance with varied gate voltages. In 2017, Xu et al. reported the fabrication of a 2D c-MOF FET device with an optimized interface contact between the active layer and dielectric layer.^[21] As the $\text{Ni}_3(\text{HITP})_2$ thin film was synthesized at the G/L interface, the membrane with a smooth top surface could be easily attached to the SiO_2/Si substrate after a stamping transfer, which allowed reduced residual at the interface. A high-quality semiconductor-dielectric interface could be created between the semiconductive c-MOF layer and the dielectric SiO_2 layer. A bottom-gate FET device with top-contact geometry was constructed after depositing patterned Au electrodes, as shown in Figure 9d. A good linear correlation between I_{ds} and V_{ds} (drain-source voltage) could be observed from the output curves in Figure 9e, which suggested an Ohmic contact between the deposited Au electrodes and 2D

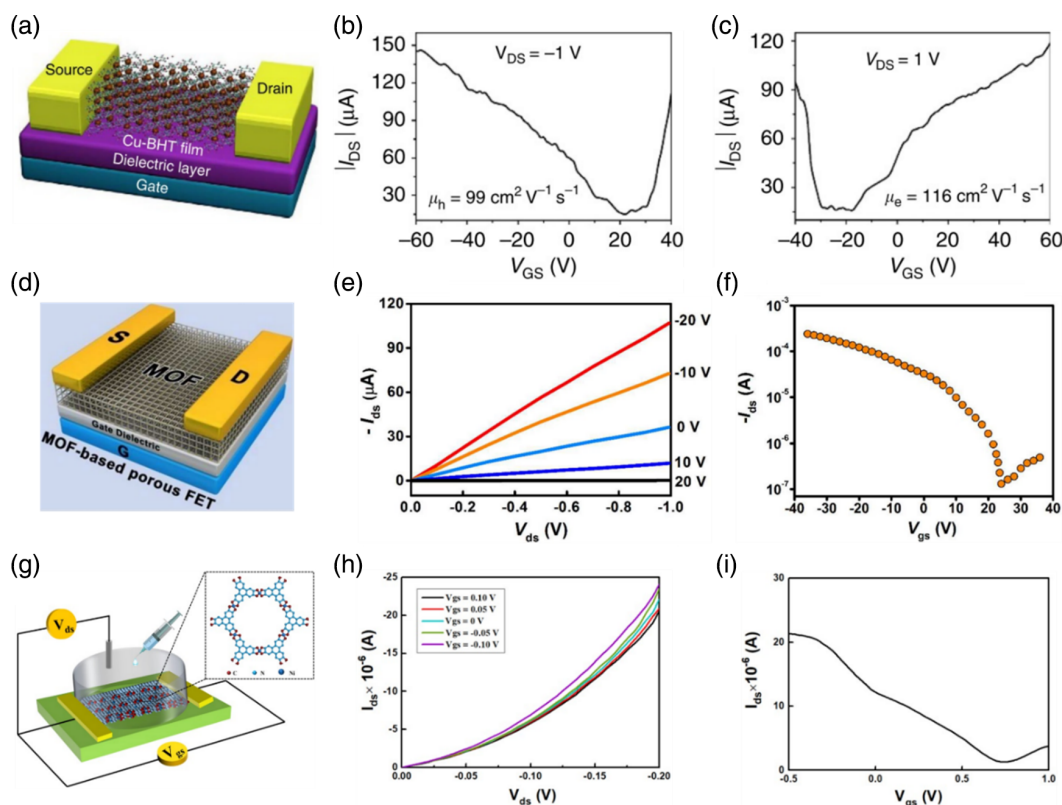


Figure 9. a) Scheme of the FET structure based on $\text{Cu}_3(\text{HTB})$ thin film. b,c) The I_{ds} versus V_{gs} transfer curves of the device. a–c) Reproduced with permission.^[7] Copyright 2015, Springer Nature. d) Scheme of the FET structure based on $\text{Ni}_3(\text{HITP})_2$ thin film. e) The I_{ds} versus V_{ds} output curves and f) I_{ds} versus V_{gs} transfer curve of the device. d–f) Reproduced with permission.^[21] Copyright 2017, American Chemical Society. g) Scheme of the liquid-gated FET device structure based on the $\text{Ni}_3(\text{HITP})_2$ thin film with phosphate-buffered saline as the liquid gate. h) The I_{ds} versus V_{ds} output curves and i) I_{ds} versus V_{gs} transfer curves of the FET device. g–i) Reproduced with permission.^[23] Copyright 2019, American Chemical Society.

c-MOF channel layer with favored charge transport. The I_{ds} versus V_{gs} transfer curve of the device (Figure 9f) exhibited a typical p-type transport behavior of the semiconducting channel layer. It indicated that holes are the majority carriers of $Ni_3(HITP)_2$ thin film. An on/off ratio of about 2000 and a hole mobility of about $\approx 48.6 \text{ cm}^2 \text{ V}^{-1} \text{ s}^{-1}$ could be extracted from the transfer curve. Moreover, a subthreshold swing value of $2.4 \text{ V decade}^{-1}$ and an interface defect density of about $8.2 \times 10^{12} \text{ cm}^{-2}$ of the fabricated device were calculated, which revealed a low defect density at the semiconductor–dielectric interface. Duan et al. reported the $Ni_3(HITP)_2$ -based FET device via “in situ” growing the 2D c-MOF membrane on the device channel.^[23] Typically, Au/Ti electrodes were pre-deposited on the SiO_2/Si substrate surface via magnetron sputtering, where the substrate was pretreated by ozone to enhance the interaction with the c-MOF films. After directly growing $Ni_3(HITP)_2$ thin films on the treated substrate via L/S interfacial synthesis, the FET device with a bottom-contact geometry could be realized. A charge mobility of $45.4 \text{ cm}^2 \text{ V}^{-1} \text{ s}^{-1}$, an on/off ratio of about 2290, and a low subthreshold swing value of $1.3 \text{ V decade}^{-1}$ were extracted for the fabricated device. The high device performance was believed to be contributed by the good contact at the semiconductor–electrode interface as well as the intrinsic superior properties of $Ni_3(HITP)_2$ c-MOFs. Moreover, they also fabricated a liquid-gated FET device based on the $Ni_3(HITP)_2$ with phosphate-buffered saline as the liquid gate, as shown in Figure 9g. The I_{ds} versus V_{ds} (Figure 9h) and I_{ds} versus V_{gs} (Figure 9i) curves demonstrated the field-effect performance of the device under liquid conditions.

The extended conjugated structures and the tunable bandgaps make 2D c-MOFs attractive active channel layers for FETs. The so-far-reported 2D c-MOF-based FET devices were mainly constructed with their film samples that were synthesized by the LIAS method. This is due to the fact that the high crystallinity and large-area, continuous surfaces of these thin film samples are in favor of interface contact and device integration. However, the figure-of-merit (e.g., on/off ratios) of currently demonstrated FETs was very low due to that the employed 2D c-MOF samples contained appreciable defects of grain boundaries and doping. Several challenges concerning the synthetic 2D c-MOFs and device fabrication remain to be addressed. For example, devices based on high-quality c-MOF thin films with strictly controlled thickness were still required for exploring the intrinsic charge transport behavior as well as the interlayer-interaction-induced properties. The device structure could be further optimized via employing metal electrodes with suitable work functions.

4.2. Chemiresistive Sensors

The porous network structure of MOFs offers them with high specific surface area and abundant active sites for capturing small molecules or ions, which makes them the promising building blocks of sensors.^[85] However, the insulating nature of most MOF materials generally leads to sensors with inefficient signal transduction. The intrinsic high electrical conductivity of 2D c-MOFs allows them to utilize the varied electrical resistance as the response to the variation of the surrounding chemical environment, thereby enabling fast electrical signal transduction for

sensing. Various chemiresistive sensors were constructed and explored based on 2D c-MOF films.

One representative example was reported by Dincă et al., where a chemiresistive sensor based on $Cu_3(HITP)_2$ film was utilized to detect ammonia (NH_3) vapor.^[25] The device was fabricated via drop-casting the suspension of 2D c-MOFs on the substrate with pre-deposited Au electrodes. As exhibited in Figure 10a, the device was placed in a chamber, where a continuous gas flow could be injected at a constant rate. The composition of the gas stream could be switched between pure nitrogen (N_2) gas and the mixture of NH_3/N_2 to change the surrounding chemical environment. After applying a constant voltage of 100 mV, a stable current value of the $Cu_3(HITP)_2$ device could be observed upon exposure to pure N_2 , while a sharp elevation of the output current would be appeared after replacing the N_2 by NH_3 mixture (Figure 10b). The current would recover to the initial level when pure N_2 flow was injected again, and this reversible cycle could be reproduced more than 10 times. Here, the lowest NH_3 concentration for detection is 0.5 parts per million (ppm) in the inert N_2 atmosphere. While in the air condition with a relative humidity of 60%, the $Cu_3(HITP)_2$ device could still work reliably and the detected NH_3 concentration lowered to 5 ppm. However, the sensor based on $Ni_3(HITP)_2$ did not exhibit an observable response after exposure to the NH_3 atmosphere, which suggested that the metal nodes play an important role in the functionality of 2D c-MOFs. Later on, Mirica et al. reported the fabrication of chemiresistive sensors based on $M_3(HHTP)_2$ ($M = Cu$ and Ni) c-MOFs for gas detection.^[82] The photograph and the scheme of the device architecture are displayed in Figure 10c, where the interdigitated graphite electrodes were fabricated on a shrinkable polymeric film and defined by directly drawing with a commercial pencil. The HHTP-based c-MOF was straightly assembled into the device via immersing the prepared shrinkable film into the reaction solution. This straightforward L/S interfacial synthesis approach allowed the Ohmic contact with low resistivity between electrodes and 2D c-MOF thin films. The obtained sensor devices were utilized to detect toxic gases, including NH_3 , hydrogen sulfide (H_2S), and nitric oxide (NO). After exposing to different kinds of gases, the devices based on different c-MOF layers exhibited distinctive responses. The resistivity of $Cu_3(HHTP)_2$ -based sensor showed a slight increase after being surrounded by NH_3 , while no obvious variation was observed for the $Ni_3(HHTP)_2$ -based one. Consistent increases in conductivity of both devices were revealed upon exposure to NO, but showed different changing rates. After utilizing H_2S as the detecting object, the resistivity increase of both devices was demonstrated, while the $Ni_3(HHTP)_2$ sensor showed a more dramatic variation compared to $Cu_3(HHTP)_2$ one. Principal component analysis (PCA), which is a commonly used data analysis technique to classify data according to their similarity, was conducted to explore the function of the sensor devices in differentiating the gaseous analytes. Three gases and water were resolved based on two principal components (labeled as PC1 and PC2), as shown in Figure 10d. The same group also reported the integration of $M_3(HHTP)_2$ ($M = Fe, Co, Ni,$ and Cu) into functional gas sensors via mechanical abrasion.^[81] Hybrids of $M_3(HHTP)_2$ and graphite were employed as the active materials to improve the electrical contacts of c-MOF crystallites/metallic electrodes and individual c-MOF crystallites/c-MOF

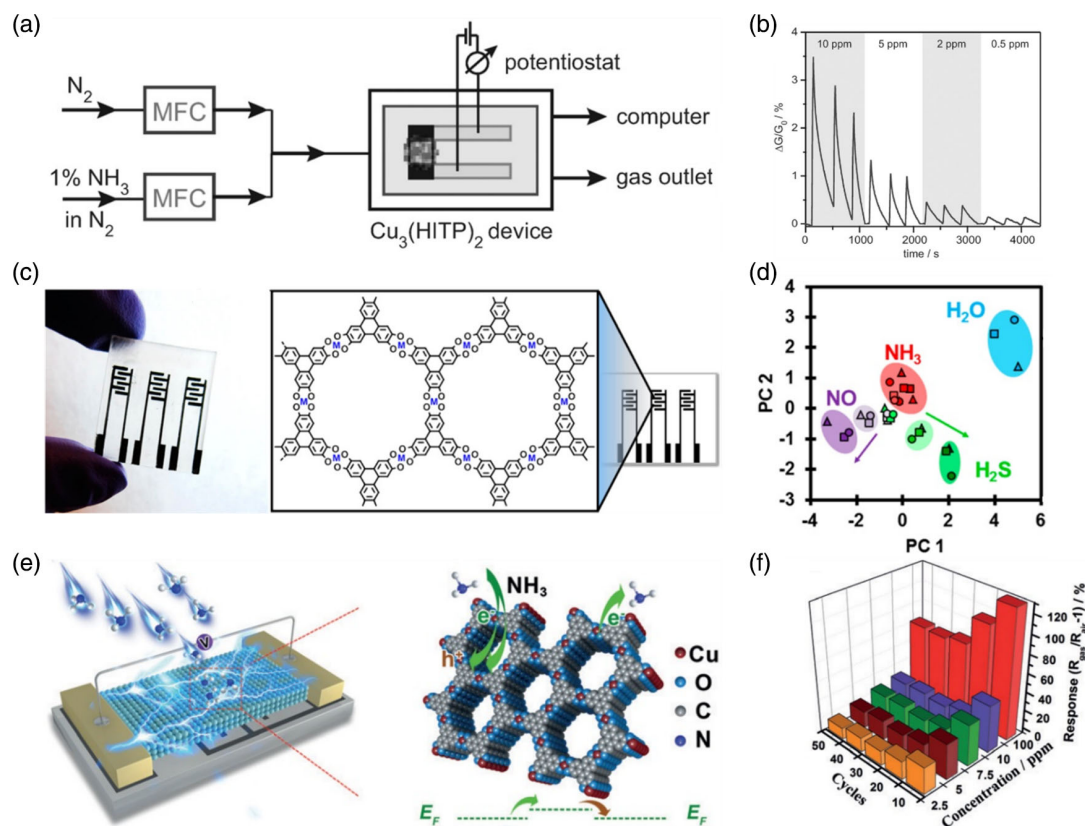


Figure 10. a) Scheme of the experimental setup for chemiresistive sensing based on $\text{Cu}_3(\text{HITP})_2$ film. b) Chemiresistive responses toward NH_3 environment with different concentrations. a,b) Reproduced with permission.^[25] Copyright 2015, Wiley-VCH. c) The photograph and the scheme of the fabricated device architecture via direct drawing. d) PCA result of the acquired response data, NH_3 marked in red, NO marked in purple, H_2S marked in green, and H_2O marked in blue. c,d) Reproduced with permission.^[82] Copyright 2016, American Chemical Society. e) Scheme of the gas sensing process (left) and possible sensing mechanism for $\text{Cu}_3(\text{HITP})_2$ -based chemiresistive sensors toward NH_3 . f) Chemiresistive response comparison of the device toward NH_3 with different concentrations at various cycles. e,f) Reproduced with permission.^[27] Copyright 2017, Wiley-VCH.

crystallites. The fabricated devices exhibited a chemiresistive response toward gaseous analytes of NH_3 , NO , and H_2S in ppm levels. They also proposed the fabrication of flexible sensors based on electronic textiles.^[48] Such L/S-based method enabled $\text{Ni}_3(\text{HHTP})_2$ and $\text{Ni}_3(\text{HITP})_2$ samples to directly integrate into fabrics to form flexible conductive textiles. The as-fabricated chemiresistive devices could simultaneously realize the functions of sensing, capture, and filtration of gaseous analytes. The chemiresistive ability of NO , H_2S , and H_2O gases at ppm levels was also demonstrated, and the detection response could be maintained at a relative humidity of 18%. Theoretical detection limits for NO of 0.16 ppm and H_2S of 0.23 ppm were demonstrated. Recently, Mirica et al. also realized a series of chemiresistive sensors that were functionalized by phthalocyanine-derivatives-based 2D c-MOF layers, including $\text{M}_2[\text{NiPc}(\text{OH})_8]$ and $\text{M}_2[\text{NiNPc}(\text{OH})_8]$ ($\text{M} = \text{Cu}$ and Ni).^[41] The 2D c-MOFs were synthesized via the solvothermal method and pressed into pellets for fabricating devices. Gaseous analytes with concentrations at sub-ppm to ppb levels could trigger the resistance change of the fabricated devices, which indicated an improved detection performance compared to the previous works.^[48] The limit of detection (LOD) for NH_3 of

0.31–0.33 ppm, H_2S of 19–32 ppb, and NO of 1.0–1.1 ppb were achieved after the sensors were derived by 0.01–1.0 V voltage and 1.5 min exposure duration. In another recent work from Dinca et al., they reported the fabrication of a $\text{Cu}_3(\text{HIB})_2$ -based chemiresistive platform toward CO_2 detection.^[86] The obtained device showed a good sensitivity toward small variations of ambient CO_2 concentration in the range of 400–1000 ppm.

In addition, Xu et al. also developed the chemiresistive sensors based on $\text{Cu}_3(\text{HHTP})_2$ for detecting NH_3 at room temperature (Figure 10e) and investigated the possible sensing mechanism.^[27] The employed $\text{Cu}_3(\text{HHTP})_2$ thin films were directly formed on the substrates via the spray-based L/S interfacial synthesis methods, which showed high compatibility toward device fabrication. As shown in Figure 10f, the fabricated $\text{Cu}_3(\text{HHTP})_2$ devices exhibited a high resistance change (about 129% on average) after exposed to 100 ppm NH_3 atmosphere. The detecting mechanism of the $\text{Cu}_3(\text{HHTP})_2$ sensors was explored via analyzing the structural variations of 2D c-MOF thin films before and after exposure to NH_3 . The spectra results indicated the formation of strong interaction between NH_3 molecules and $\text{Cu}_3(\text{HHTP})_2$ networks, which was deemed as the root cause for the favorable response. The ultraviolet

photoelectron spectroscopy results suggested a 1.13 eV increase of the Fermi level of the $\text{Cu}_3(\text{HHTP})_2$ layer after NH_3 adsorption, which agreed well with the variation of a p-type semiconductor doped by n-type materials.^[87] Thus, the connection of p-type $\text{Cu}_3(\text{HHTP})_2$ layer and n-type analyte NH_3 led to the recombination of the hole and the doped electron, further reducing the concentration of majority carrier (hole) in $\text{Cu}_3(\text{HHTP})_2$ and causing the resistance increases of the chemiresistive sensor. For further probing the detection mechanism, Martí-Gastaldo et al. combined both experimental measurements and computational simulations to investigate the sensor performance of $\text{Cu}_3(\text{HHTP})_2$ -based devices.^[24] Here, the 2D c-MOF layers were synthesized from the G/L-based LIAS method. Their results suggested that the sensing response toward gas molecules originated from the coordination effect between the gaseous guests and the metal sites in the 2D c-MOF layers, which led to the alteration of the electrical conductivity. The strong interaction between NH_3 and $\text{Cu}_3(\text{HHTP})_2$ networks was examined by Kelvin probe measurements and infrared (IR) spectroscopy, which indicated an observable change of work function and appearance of their coordination interaction, respectively. The simulation results indicated that the electronic structure of 2D c-MOFs was slightly distorted owing to the coordination with gas molecules, which further led to the variation of the bandgap of the solid. Kitagawa et al. employed a dual-ligand 2D c-MOF layer, i.e., $\text{Cu}_3(\text{HHTP})(\text{HHB})$, to fabricate chemiresistive sensors, which behaved good discrimination performance toward NH_3 with concentrations ranging from 1 to 100 ppm.^[88] Here, the strong coordination effect between Cu ions and NH_3 molecules was

also confirmed by IR and powder X-ray diffraction, which was deemed as the root cause for the good selectivity of Cu c-MOFs toward NH_3 .

The chemiresistive sensors based on 2D c-MOF could also be employed to discriminate other substances, such as volatile organic compounds (VOCs) and ions. Dincă et al. demonstrated the fabrication of a cross-reactive sensor array functionalized by structurally analogous triphenylene-based 2D c-MOF thin films, i.e., $\text{Cu}_3(\text{HHTP})_2$ and $\text{M}_3(\text{HITP})_2$ ($\text{M} = \text{Cu}$ and Ni).^[26] For fabricating chemiresistive sensor devices, the active layers were formed via drop-casting or mechanical drawing of the 2D c-MOF bulks. The obtained device enabled to differentiate five different categories of VOCs, including aliphatic, alcohols, amines, aromatic hydrocarbons, and ketones/ethers, where each category contains three or four different molecules. The devices were fabricated by drop-casting or mechanical drawing 2D c-MOF layers on substrates with pre-prepared Au electrodes. The sensing responses of three different devices toward 16 different molecules at 200 ppm concentration suggested distinctive variations of resistance in direction and/or magnitude, as shown in **Figure 11a**. It can also be observed that exposure to polar VOCs generally led to a sharp variation in resistance of the devices, while no apparent response could be observed toward aliphatic hydrocarbons. PCA was conducted to analyze the acquired response data and yielded groupings of the data from analytes with the same functional group (**Figure 11b**). The inner mechanism was supposed to be contributed by charge transfer and hydrogen bonding between 2D c-MOFs and VOC molecules. Behrens et al. reported a chemiresistive sensor toward methanol

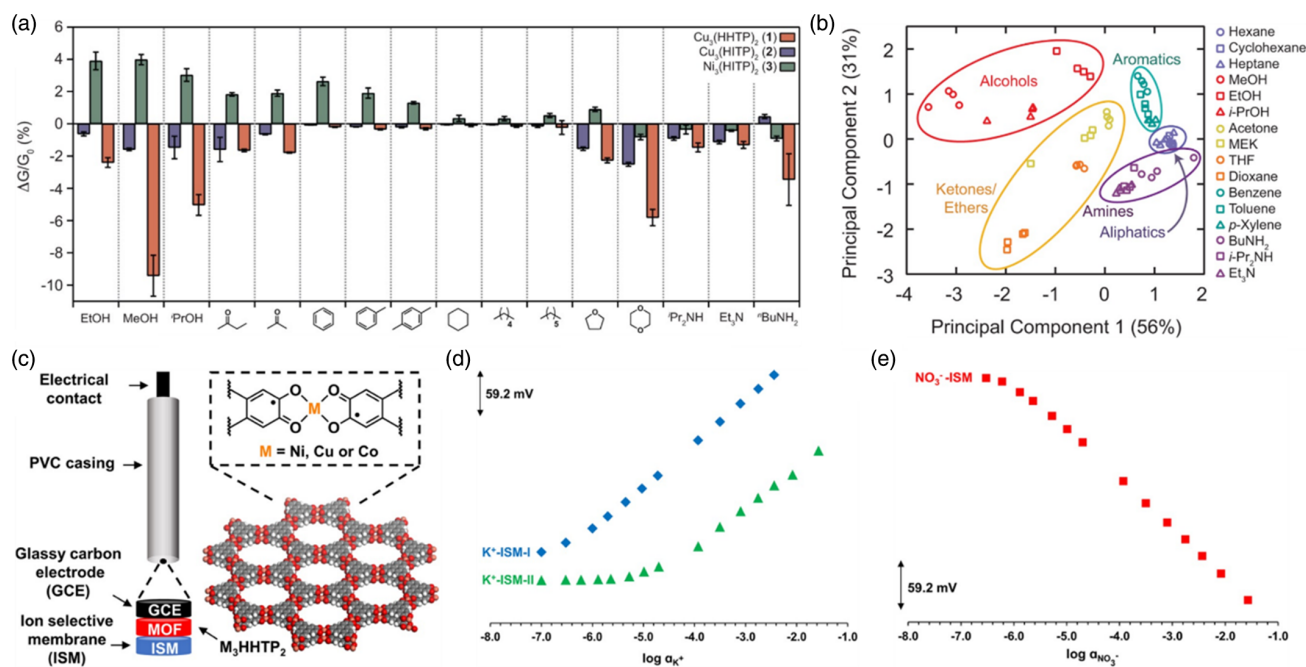


Figure 11. a) Sensing responses of the cross-reactive sensor array toward 16 representative molecules from five categories of VOCs. b) PCA result of the acquired response data, showing groupings of the data from analytes with the same functional group. a,b) Reproduced with permission.^[26] Copyright 2015, American Chemical Society. c) Schematic illustration of the ion-to-electron transducers based on a glassy carbon electrode with a 2D c-MOF layer and an ion-selective membrane layer. Sensing response of the fabricated devices toward d) K^+ and e) NO_3^- . c-e) Reproduced with permission.^[83] Copyright 2018, American Chemical Society.

based on $\text{Cu}_3(\text{HHTP})_2$ film, which was formed via spray-coating its water dispersion on the target substrate.^[89] Recently, our group fabricated polarity-selective chemiresistors based on polycrystalline $\text{Ni}_2[\text{MPc}(\text{NH})_8]$ ($M = \text{Cu}$ or Ni) thin films for detecting water and VOCs.^[90] The centimeter-scale 2D c-MOF thin films were synthesized via the LIAS approach at the L/S (dimethyl sulfoxide/ SiO_2) interface and the resultant samples showed high electrical conductivity of $0.3\text{--}0.6 \text{ S cm}^{-1}$. The sensors were then fabricated via thermally evaporated gold electrodes on the film surface. The as-synthesized $\text{Ni}_2[\text{MPc}(\text{NH})_8]$ thin films (and the films integrated into the sensors) could be modified by various insulating silanes, which enabled the surface wettability to be modulated from hydrophobic to hydrophilic. Here, the solutions of silanes comprised of different functional groups (including (3-aminopropyl)trimethoxysilane (APTMS), phenyltrichlorosilane (PTCS), and octadecyltrimethoxysilane (OTMS)) were spin-coated on the film surface to realize the surface modification. During the chemiresistive sensing of water, the functionalized surface could suppress the diffusion of water molecules into the 2D c-MOF backbone, thereby greatly improving the recovery process ($\approx 10 \text{ s}$ at $600 \text{ ppm H}_2\text{O}$) compared with the device based on pristine sample ($\approx 50 \text{ s}$). An improved sensing performance toward high-polarity molecules, i.e., methanol, was also demonstrated based on the samples functionalized by hydrophobic aliphatic alkyl chains, which showed a faster response and recovery progress of 36 and 13 s, respectively, compared to the performance of the pristine one (recovery time $> 50 \text{ s}$). Moreover, an ultralow LOD of 10 ppm was realized toward methanol, which was demonstrated as the most efficiently detected molecule among alcohols. It was originated from the higher polarity and higher dielectric constant of molecules compared to other alcohol molecules, which induced the strongest affinity toward the $\text{Ni}(\text{NH})_4$ -linkage of $\text{Ni}_2[\text{MPc}(\text{NH})_8]$ frameworks. Sensor devices based on 2D c-MOF thin films could also be utilized to detect dissolved ions and molecules. Mirica et al. reported the fabrication of potentiometric sensors based on $\text{M}_3(\text{HHTP})_2$ ($M = \text{Ni}, \text{Cu}, \text{and Co}$),^[83] where the active layer was obtained via drop-casting 2D c-MOF samples on a glassy carbon electrode. A layer of ion-selective membrane was then covered on the top to construct the ion-to-electron transducer, as shown in Figure 11c. The fabricated devices exhibited observable responses toward K^+ (Figure 11d) and NO_3^- (Figure 11e). The results indicated a near-Nernstian slope of $54.1\text{--}58.2 \text{ mV s}^{-1}$ and an LOD of $10^{-6}\text{--}10^{-7} \text{ M}$. Zhang et al. employed the chemiresistive sensors based on L/L interfacial synthesized $\text{Cu}_3(\text{HHTX})_2$ layers to detect paraquat, which showed a detection limit at 10^{-8} M level.^[38]

The numerous chemiresistive sensors were successfully fabricated based on 2D c-MOF thin films in the last few years, and these devices exhibited remarkable performance toward various kinds of analytes. Most of the sensor devices were integrated from 2D c-MOF thin films synthesized by the LIAS method, owing to the large area, high crystallinity, and tunable thickness. Particularly, the L/S interfacial synthesis was the most commonly used approach among the three LIAS methods. Such process enabled the realization of large-area, thin films on solid substrates, which showed high compatibility for direct device fabrication. However, analogous to FETs, the quality of the functional films still needed to be addressed for eliminating the

effect from lattice defects. Devices based on high-quality samples were required to reliably analyze the sensing performance. Primary investigations toward the sensing mechanisms were carried out and provided several convincing conclusions. However, the fundamental comprehension of chemiresistive behaviors of 2D c-MOFs with different metal nodes and ligands toward analytes requires further exploration, such as the remarkable difference between Ni- and Cu-based c-MOFs toward NH_3 . Elaborating the basic mechanism could offer applicable guidelines to integrate appropriate functional layers toward target analytes.

4.3. Superconductors

Superconductivity describes a physical phenomenon that the electrical resistance of a material drops abruptly to zero when its temperature is below a critical value. One representative example is $\text{Cu}_3(\text{HTB})$ with a perfect kagome lattice (Figure 12a), which was successfully proved as a superconductor experimentally. The superconductivity of $\text{Cu}_3(\text{HTB})$ was theoretically predicted by Liu et al. in 2017.^[91] Their DFT calculations suggested a superconducting transition temperature of 1.58 K for bulk samples, while the critical temperature (T_c) of monolayer $\text{Cu}_3(\text{HTB})$ could be increased to 4.43 K. In 2018, Zhu et al. demonstrated the superconducting characteristic of $\text{Cu}_3(\text{HTB})$ thin films and revealed a transition temperature of 0.25 K.^[84] The result was extracted from the temperature-dependent resistivity of an 800 nm thick $\text{Cu}_3(\text{HTB})$ film (Figure 12b), which exhibited a sharply reduced resistance at about 0.25 K. A narrow superconducting transition region of about 20 mK was also observed, which was believed to be contributed by the high crystallinity of the sample. Magnetic field dependence of T_c was also characterized. A low-temperature shift of T_c was observed after enhancing the magnetic field, while the superconducting transition disappeared after applying a magnetic field of 0.25 T. The superconductivity of $\text{Cu}_3(\text{HTB})$ was further confirmed by the measurements of specific heat and magnetic susceptibility. In addition, another superconducting transition was observed at about 3 K during the magnetic susceptibility measurement, which was ascribed to be related to the monolayer or few-layer $\text{Cu}_3(\text{HTB})$ samples. These authors subsequently reported a comprehensive research of the superconducting behavior of $\text{Cu}_3(\text{HTB})$ and classified it as a strongly correlated unconventional superconductor.^[28] The temperature-dependent resistance measurements of the $\text{Cu}_3(\text{HTB})$ thin films were conducted after applying magnetic fields in two configurations, i.e., parallel (Figure 12c) and perpendicular (Figure 12d) to the crystal plane. The resulted curves indicated an anisotropic behavior of $\text{Cu}_3(\text{HTB})$. They also found that the superfluid density of $\text{Cu}_3(\text{HTB})$ was smaller than that of conventional superconductors in magnitude. Its unconventional superconducting behavior was ascribed to be originated from electron correlations related to spin fluctuations of the kagome lattice.

4.4. Optoelectronic Devices

Optoelectronics are devices that take advantage of the quantum mechanical effects between light and active materials, where semiconductors with suitable bandgaps are appealing materials for these optical-to-electrical and electrical-to-optical transducers.

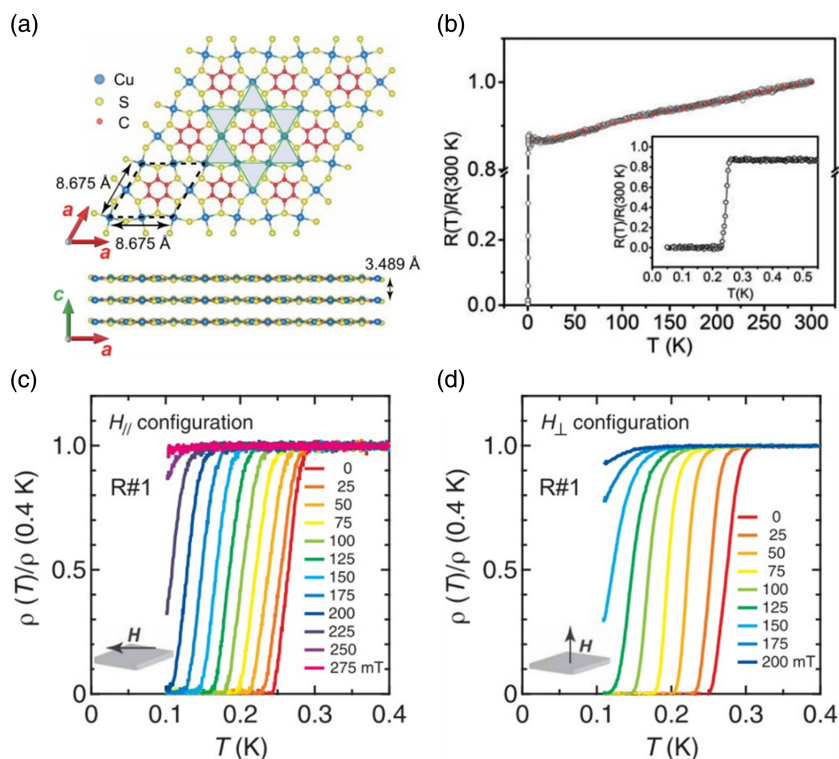


Figure 12. a) Illustration of the crystal structure of $\text{Cu}_3(\text{HTB})$ with a perfect kagome lattice. b) The temperature-dependent resistivity of an 800 nm thick $\text{Cu}_3(\text{HTB})$ film. The temperature-dependent resistance measurements of the $\text{Cu}_3(\text{HTB})$ thin film after applying magnetic fields in c) parallel and d) perpendicular directions. b) Reproduced with permission.^[84] Copyright 2018, Wiley-VCH. a,c,d) Reproduced with permission.^[28] Copyright 2021, American Association for the Advancement of Science.

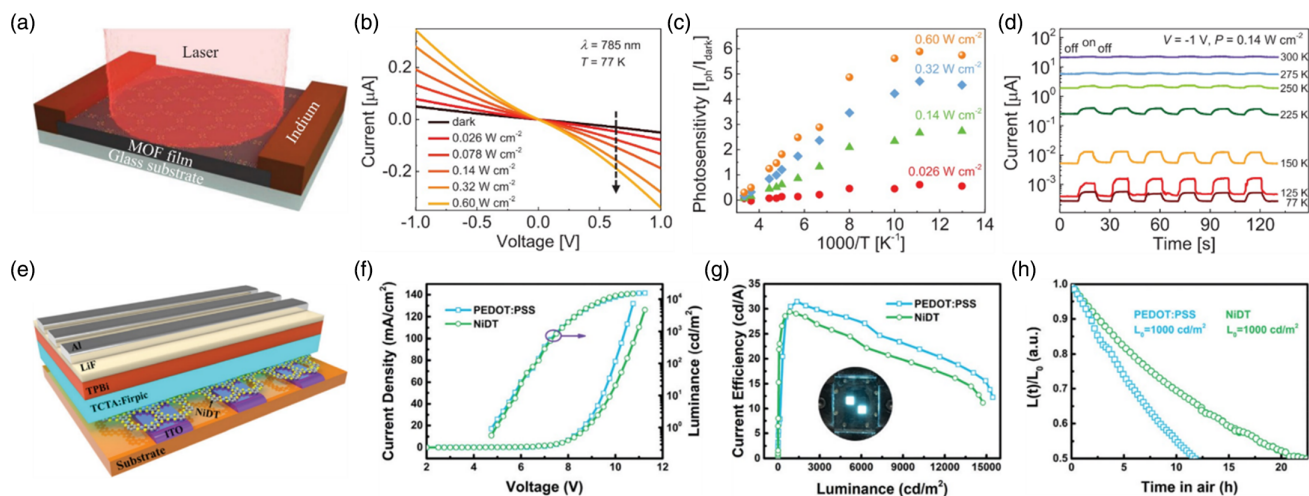


Figure 13. a) Schematic illustration of the two-terminal photodetector device based on $\text{Fe}_3(\text{HTP})_2$ thin films. b) The current–voltage curves of the device after exposure to 785 nm laser with varied power densities at 77 K. c) The temperature-dependent photosensitivity of the device illuminated by varied light strength. d) Photoswitching behavior of the device at varying temperatures after exposure to pulsed light. a–d) Reproduced with permission.^[10] Copyright 2020, Wiley-VCH. e) Schematic illustration of the blue small-molecule OLED based on $\text{Ni}_3(\text{HTB})_2$ thin films. f) The voltage-dependent current density and luminance characteristics of the devices. g) The luminance-dependent current efficiency characteristics of the devices. h) The luminance degradation characteristics of the devices. e–h) Reproduced with permission.^[92] Copyright 2020, The Royal Society of Chemistry.

Table 3. Summary of the (opto-)electronics constructed based on 2D c-MOF thin films.

(Opto-)electronics	Active layers	Synthesis	Device performances			References	
			Mobility	On/off ratio	Subthreshold swing		
FETs							
	Cu ₃ (HTB)	L/L	99 cm ² V ⁻¹ s ⁻¹ (hole) 116 cm ² V ⁻¹ s ⁻¹ (electron)	10	N/A	Zhu et al. ^[7]	
	Ni ₃ (HIB) ₂	G/L	N/A ^{a)}	N/A	N/A	Louie et al. ^[22]	
	Ni ₃ (HITP) ₂	G/L	48.6 cm ² V ⁻¹ s ⁻¹ (hole)	2000	2.4 V decade ⁻¹	Xu et al. ^[21]	
	Ni ₃ (HITP) ₂	L/S	45.4 cm ² V ⁻¹ s ⁻¹ (hole)	2290	1.3 V decade ⁻¹	Duan et al. ^[23]	
Chemiresistive sensors			Detecting substances	LOD			
	Cu ₃ (HITP) ₂	Drop-casting	NH ₃	0.5 ppm		Dincă et al. ^[25]	
	Cu ₃ (HHTP) ₂	L/S	NH ₃ , NO, H ₂ S	≈5 ppm (NH ₃); ≈20 ppm (NO); ≈40 ppm (H ₂ S)		Mirica et al. ^[81]	
	Ni ₃ (HHTP) ₂	L/S	NH ₃ , NO, H ₂ S	N/A (NH ₃); ≈20 ppm (NO); ≈20 ppm (H ₂ S)		Mirica et al. ^[81]	
	M ₃ (HHTP) ₂ /graphite (M = Fe, Co, Ni, Cu)	Ball milling	NH ₃ , NO, H ₂ S	19 ppm (NH ₃); 17 ppm (NO); 35 ppm (H ₂ S)		Mirica et al. ^[80]	
	Ni ₃ (HHTP) ₂ /textiles	L/S	NO, H ₂ S	1.4 ppm (NO); 0.23 ppm (H ₂ S)		Mirica et al. ^[48]	
	Ni ₃ (HITP) ₂ /textiles	L/S	NO, H ₂ S	0.16 ppm (NO); 0.52 ppm (H ₂ S)		Mirica et al. ^[48]	
	Ni ₂ NiPcO ₈	Solvo-thermal	NH ₃ , NO, H ₂ S	0.05–0.31 ppm (NH ₃); 0.06–1.06 ppm (NO); 2.4–32.3 ppb (H ₂ S)		Mirica et al. ^[41]	
	Cu ₂ NiPcO ₈	Solvo-thermal	NH ₃ , NO, H ₂ S	0.16–0.33 ppm (NH ₃); 0.13–1.00 ppm (NO); 1.0–18.5 ppb (H ₂ S)		Mirica et al. ^[41]	
	Cu ₃ (HIB) ₂	Hydro-thermal	CO ₂	67 ppm		Dincă et al. ^[85]	
	Cu ₃ (HHTP) ₂	L/S	NH ₃	0.5 ppm		Xu et al. ^[27]	
	Cu ₃ (HHTP) ₂	G/L	NH ₃	N/A		Martí-Gastaldo et al. ^[24]	
	Cu ₃ (HHTP)(HIB)	Hydro-thermal	NH ₃	≈0.02 ppm		Kitagawa et al. ^[87]	
	Cu ₃ (HHTP) ₂ , Cu ₃ (HITP) ₂ , Ni ₃ (HITP) ₂	Drop-casting or mechanical drawing	Aliphatic hydrocarbons, alcohols, ketones/ethers, aromatic hydrocarbons, amines	N/A		Dincă et al. ^[26]	
	Cu ₃ (HHTP) ₂	Spray-coating	Methanol	N/A		Behrens et al. ^[88]	
	Ni ₂ MPc(NH) ₈ (M = Cu, Ni)	L/S	Water, methanol, ethanol	≈10 ppm (methanol)		Dong et al. ^[89]	
	M ₃ (HHTP) ₂ (M = Ni, Cu, and Co)	Drop-casting	K ⁺ , NO ₃ ⁻	6.31 × 10 ⁻⁷ M (NO ₃ ⁻); 5.01 × 10 ⁻⁷ M (K ⁺)		Mirica et al. ^[82]	
	Cu ₃ (HHTX) ₂	L/L	Paraquat	4.1 × 10 ⁻⁸ M		Zhang et al. ^[38]	
Superconductors				Transition temperature			
	Cu ₃ (HTB)	L/L		≈0.25 K		Zhu et al. ^[83]	
	Cu ₃ (HTB)	L/L		≈0.25 K		Hashimoto et al. ^[28]	
Photodetectors			Detecting range		Specific detectivity		
	Fe ₃ (HTTP) ₂	L/L	400–1575 nm		7 × 10 ⁸ cm Hz ^{1/2} W ⁻¹ (785-nm light, 77 K)	Erbe et al. ^[10]	
OLEDs			Maximum luminance	Maximum current efficiency	Maximum external quantum efficiency		
	Ni ₃ (HTB) ₂	L/L	14730 cd m ⁻² (yellow OLED)	5.33 cd A ⁻¹ (yellow OLED); 29.4 cd A ⁻¹ (blue OLED)	4.4% (yellow OLED)	Nishihara et al. ^[91]	
Solar cells			Open-circuit voltage	Short-circuit current density	Fill factor	Power conversion efficiency	
	Cu ₃ (HTB)/perovskite	L/L	0.985 V	20.47 mA cm ⁻²	70.1%	14.13%	Wang et al. ^[92]
	Cu ₃ (HTB)/PbS quantum dots	L/L	0.591 V	23.87 mA cm ⁻²	58.5%	8.25%	Wang et al. ^[92]
	Cu ₃ (HTB)/PTB7:PCBM	L/L	0.744 V	15.02 mA cm ⁻²	65.8%	7.35%	Wang et al. ^[92]

Table 3. Continued.

(Opto-)electronics	Active layers	Synthesis	Device performances			References
			Mobility	On/off ratio	Subthreshold swing	
FETs			Seebeck coefficient	Thermal conductivity	ZT	
Thermoelectrics	Ni ₃ (HTP) ₂	Hydro-thermal	-11.9 μV K ⁻¹	0.21 W m ⁻¹ K ⁻¹	1.19 × 10 ⁻³	Dincă et al. ^[11]
	Ni ₃ (PTC)	Solvo-thermal	-47.0 μV K ⁻¹	0.2 W m ⁻¹ K ⁻¹	3 × 10 ⁻³	Zhu et al. ^[29]

^{a)}N/A: not applicable.

2D c-MOF thin films featured with tunable bandgaps have been applied in several optoelectronic devices, including photodetectors,^[10] organic light-emitting diodes (OLED),^[92] and photovoltaic solar cells.^[93]

In 2020, we demonstrated the two-terminal photodetectors based on the semiconducting Fe₃(HTTP)₂ thin film.^[10] As illustrated in **Figure 13a**, the Fe₃(HTTP)₂ thin film was supported by a glass substrate, and indium was employed as the electrode. The fabricated photodetectors exhibited a broadband photoresponse, where the wavelengths of detected light ranged from ultraviolet to near-infrared (400–1575 nm). In contrast to the results at room temperature, a highly improved photodetection performance at 77 K (liquid nitrogen temperature) of the device was confirmed by the temperature dependence measurements. Drastically upgraded figures of merit of the device were observed after cooling, including an elevated specific detectivity, optimized noise equivalent power, enhanced photosensitivity, and voltage responsivity. **Figure 13b** displayed the typical current–voltage curves of the device upon illuminating by 785 nm laser with varied power densities at 77 K, which showed an increased photocurrent with increasing the photon density. The temperature-dependent photosensitivity measurements with temperatures ranging from 77 to 300 K were also conducted to clarify the effect brought by temperature. As shown in **Figure 13c**, the outcomes suggested an observable negative correlation, which was ascribed to the narrow IR bandgap nature of the Fe₃(HTTP)₂ thin film. Typically, narrow bandgap would be in favor of thermally generating free charge carriers at room temperature, while cooling down the temperature would reduce the thermally activated band-to-band population and thereby improve the photodetection performance. Moreover, the photo-switching behavior of the device was also investigated upon illumination of pulsed 785 nm laser at varying temperatures. A reproducible and stable photoswitching performance was demonstrated, and response times were extracted as 2.3 s of rising process and 2.15 s of decay process at 77 K, as shown in **Figure 13d**.

Nishihara et al. fabricated OLED devices with 2D c-MOF thin films as a hole buffer layer.^[92] The L/L interfacial synthesized Ni₃(HTB)₂ thin films were transferred on indium tin oxide (ITO) glass substrates for integrating OLEDs, as shown in **Figure 13e**. A conventional OLED device based on poly(3,4-ethylenedioxythiophene) polystyrene sulfonate (PEDOT:PSS) was employed for comparison. **Figure 13f** exhibited the voltage-dependent current density and luminance characteristics of the 2D c-MOF OLED and conventional OLED. The two kinds of devices exhibited comparable maximum current efficiencies, which

were extracted as 29.4 cd A⁻¹ of the 2D c-MOF device and 31.4 cd A⁻¹ of the conventional device (**Figure 13g**). In addition, the 2D c-MOF device showed improved stability compared to the conventional one (**Figure 13h**). These results demonstrated the potential of Ni₃(HTB)₂ thin films as an appealing fluorescent building block in OLEDs. 2D c-MOF thin films could also serve as conductive layers in solar cells owing to their low-consumption synthesis and high flexibility. Wang et al. employed Cu₃(HTB) thin films as transparent electrodes of solar cells for taking advantage of their high electrical conductivity (2500 S cm⁻¹), high transmittance (82%), and handy solution processing.^[93] The fabricated Cu₃(HTB) solar cells exhibited comparable performance toward the devices functionalized by traditional ITO electrodes.

4.5. Others

In addition to previously mentioned (opto-)electronic devices, 2D c-MOF thin films also exhibited great application potential in other electronic applications, such as thermoelectrics.^[11,29] Dincă et al. investigated the thermoelectric properties of Ni₃(HTP)₂ sample, which was recognized as an n-type thermoelectric material with a negative Seebeck coefficient of -11.9 μV K⁻¹ at room temperature.^[11] The prepared Ni₃(HTP)₂ device exhibited an ultralow thermal conductivity value of about 0.21 W m⁻¹ K⁻¹ owing to the porous network structure with strong phonon scattering ability. Taking advantage of its high electrical conductivity, the ZT (describe the thermoelectric conversion efficiency) of Ni₃(HTP)₂ could reach 1.19 × 10⁻³ at room temperature. The acquired value is about 17 times larger than the ZT of traditional MOF [7,7,8,8-tetracyanoquinodimethane-infiltrated Cu₃(benzene-1,3,5-tricarboxylate)₂]-based device. Zhu et al. explored the thermoelectric behavior of Ni₃(PTC) samples, which were revealed as p-type thermoelectric materials.^[29] The Seebeck coefficient and thermal conductivity were extracted as -47.0 μV K⁻¹ and 0.2 W m⁻¹ K⁻¹, respectively, which further led to a high ZT value of 3 × 10⁻³ at room temperature.

As described in **Table 3** and 2D c-MOF film samples achieved by LIAS methods have been widely employed as the active materials for versatile (opto-)electronics. In view of their compatibility with the existing device-integrating technology, high-performance applications based on 2D c-MOFs were demonstrated, such as high-mobility FETs, low-LOD chemiresistive sensors, broadband-photoresponse photodetectors, and large-ZT thermoelectrics. However, the in-depth exploration of the fundamental mechanisms behind the device characteristics still requires more effort for integrating suitable device

structures. Rationally employed 2D c-MOF active layers with suitable electronic structures were also required to boost the device figure-of-merits via constructing appropriate band structures.

5. Summary and Outlook

In this review, we briefly introduced the molecular design of 2D c-MOFs and the fundamental understanding of their structure–(opto)electronic property relationship. Currently, unique 2D c-MOFs with multifarious characteristics have been rising, such as $\text{Cu}_3(\text{HTB})$ with high electrical conductivity and $\text{Fe}_3(\text{HTTP})_2$ with high charge carrier mobility. To facilitate device integrations, various synthesis routes toward 2D c-MOF films were outlined in this review. Generally, exfoliation and ERA methods are featured with high yielding, but suffer from the drawbacks of low controllability and uniformity. In contrast, bottom-up synthesis methods possess an advantage in the controllable growth of 2D c-MOFs and are apt to form large-area high-quality film samples with well-controlled thickness. LIAS approaches are the most commonly employed bottom-up methods to synthesize 2D c-MOF thin films with thickness down to monolayer or few layer. However, owing to the lack of precise controllability in crystal growth kinetics, the obtained thin films are generally polycrystalline samples formed by nanometer-scale domains, which severely restricts the establishment of reliable structure–property relationships. CVD approach is known as a highly appealing synthesis method owing to its superiorities in the controllability of the elementary crystal growth processes. Recent advances have demonstrated the potential of CVD in synthesizing 2D c-MOF film samples. Although the currently acquired samples may not yet meet our expectations of high-quality thin films, we still believe that the high- or single-crystallinity, large-size 2D c-MOF film samples could be achieved based on rationally designed CVD growth strategies.

Taking advantage of facile device integration of the thin film samples, a broad range of (opto-)electronic devices functionalized by 2D c-MOF thin films have been established. These 2D c-MOF film-based devices cover FETs, chemiresistive sensors, superconductors, photodetectors, and thermoelectrics, which are discussed in detail in this review. Owing to the unique structural characteristics and intrinsic electrical properties, remarkable progress has been achieved, thus demonstrating the great potential of 2D c-MOF thin films as the active layer of the next-generation (opto-)electronics. However, further device investigations based on varied device structures are required for in-depth probing of the fundamental mechanisms.

Despite the remarkable progress of 2D c-MOF thin films in the areas of syntheses and (opto-)electronic applications, several grand challenges are still remained to be addressed for promoting the further developments of this conductive material family. 1) The first challenge is to acquire a precise and reliable structure–property relationship of 2D c-MOFs to guide the property tuning and device architecture designing. Owing to the polycrystallinity nature of the synthesized thin-film samples, the currently obtained electronic properties were analyzed upon the contributions of lattice defects such as grain boundaries and edges. Therefore, studies based on 2D c-MOF films with large domain size (micrometer- or millimeter-scale) and

negligible lattice defects were urgently required for an explicit exploration of the charge transport behavior as well as an in-depth understanding of the basic mechanism behind the device performance.

(2) The second challenge is to develop a rational synthesis protocol for acquiring sizeable 2D c-MOF single crystals, which allows the experimental demonstration of the theoretically predicted unique properties, such as the topological insulator nature of monolayer $\text{Ni}_3(\text{HTB})_2$ single crystal. Generally, the currently reported bottom-up synthesis methods lead to polycrystalline 2D c-MOF samples with widespread grain boundaries. The root cause lies in the inferior controllability of the crystal growth kinetics during the synthesis. We believe that CVD approaches with rationally designed growth strategies have a great potential to address this challenge owing to its superior controllability in the elementary growth steps, e.g., altering the interface interaction between substrates and material layers during growth to trigger the 2D anisotropic growth behavior of the material. Although the CVD growth of 2D c-MOF films would suffer from a few limitations in terms of employing suitable reactants and growth temperatures, the CVD approach could exhibit its great potential in the controllable and universal synthesis of high-quality 2D c-MOF samples in a near future. Moreover, 2D c-MOF samples are directly formed on target substrates via CVD methods, which enables to avoid the film transfer process as well as the resulting impurities and cracks.

(3) The third challenge is to design new functions based on 2D c-MOF thin films. For example, it is appealing to develop 2D van der Waals heterostructures based on different 2D c-MOFs or 2D c-MOF with other inorganic 2D materials (e.g., graphene and MoS_2) for driving novel physical and chemical characteristics. The design of 2D c-MOFs with multicomponent (e.g., multimetals, multiligands, multipores) feature is also a promising way to extend application potential and explore unpredicted properties. Moreover, fabricating 2D c-MOFs with a controlled layer stacking model or twisted angle can also offer researchers a promising platform to probe unique electronic or spintronic features.

Although a huge gap still requires to be addressed for realizing the commercialization of the batch production and practical application of 2D c-MOF thin films, we believe that this rising material family will serve as one significant building block to functionalize the next-generation (opto-)electronic devices in the near future.

Acknowledgements

The authors thank the financial support from the ERC Starting Grant (FC2DMOF, No. 852909), Coordination Networks: Building Blocks for Functional Systems (SPP 1928, COORNETs), EU Graphene Flagship (GrapheneCore3, No. 881603), DFG project (CRC 1415, No. 417590517), and the German Science Council, Center for Advancing Electronics Dresden (EXC1056). R.D. thanks Taishan Scholars Program of Shandong Province (tsqn201909047). J.L. appreciates the support from the Alexander von Humboldt Foundation.

Open access funding enabled and organized by Projekt DEAL.

Conflict of Interest

The authors declare no conflict of interest.

Keywords

(opto-)electronics, conductive MOFs, CVD, exfoliation, interfacial synthesis, thin film, two-dimensional metal–organic frameworks

Received: November 23, 2021

Revised: January 20, 2022

Published online:

- [1] Q. Yang, Q. Xu, H. L. Jiang, *Chem. Soc. Rev.* **2017**, *46*, 4774.
- [2] E. D. Bloch, W. L. Queen, R. Krishna, J. M. Zadrozny, C. M. Brown, J. R. Long, *Science* **2012**, *335*, 1606.
- [3] J. Liu, C. Wöll, *Chem. Soc. Rev.* **2017**, *46*, 5730.
- [4] H. Furukawa, K. E. Cordova, M. O’Keeffe, O. M. Yaghi, *Science* **2013**, *341*, 1230444.
- [5] L. S. Xie, G. Skorupskii, M. Dincă, *Chem. Rev.* **2020**, *120*, 8536.
- [6] M. Wang, R. Dong, X. Feng, *Chem. Soc. Rev.* **2021**, *50*, 2764.
- [7] X. Huang, P. Sheng, Z. Tu, F. Zhang, J. Wang, H. Geng, Y. Zou, C. A. Di, Y. Yi, Y. Sun, W. Xu, D. Zhu, *Nat. Commun.* **2015**, *6*, 7408.
- [8] S. Chen, J. Dai, X. C. Zeng, *Phys. Chem. Chem. Phys.* **2015**, *17*, 5954.
- [9] R. Dong, P. Han, H. Arora, M. Ballabio, M. Karakus, Z. Zhang, C. Shekhar, P. Adler, P. S. Petkov, A. Erbe, S. C. B. Mannsfeld, C. Felser, T. Heine, M. Bonn, X. Feng, E. Cánovas, *Nat. Mater.* **2018**, *17*, 1027.
- [10] H. Arora, R. Dong, T. Venanzi, J. Zscharschuch, H. Schneider, M. Helm, X. Feng, E. Cánovas, A. Erbe, *Adv. Mater.* **2020**, *32*, 1907063.
- [11] L. Sun, B. Liao, D. Sheberla, D. Kraemer, J. Zhou, E. A. Stach, D. Zakharov, V. Stavila, A. A. Talin, Y. Ge, M. D. Allendorf, G. Chen, F. Léonard, M. Dincă, *Joule* **2017**, *1*, 168.
- [12] R. Dong, Z. Zhang, D. C. Tranca, S. Zhou, M. Wang, P. Adler, Z. Liao, F. Liu, Y. Sun, W. Shi, Z. Zhang, E. Zschech, S. C. B. Mannsfeld, C. Felser, X. Feng, *Nat. Commun.* **2018**, *9*, 2637.
- [13] M. Hmadeh, Z. Lu, Z. Liu, F. Gándara, H. Furukawa, S. Wan, V. Augustyn, R. Chang, L. Liao, F. Zhou, E. Perre, V. Ozolins, K. Suenaga, X. Duan, B. Dunn, Y. Yamamoto, O. Terasaki, O. M. Yaghi, *Chem. Mater.* **2012**, *24*, 3511.
- [14] J. H. Dou, M. Q. Arguilla, Y. Luo, J. Li, W. Zhang, L. Sun, J. L. Mancuso, L. Yang, T. Chen, L. R. Parent, G. Skorupskii, N. J. Libretto, C. Sun, M. C. Yang, P. V. Dip, E. J. Brignole, J. T. Miller, J. Kong, C. H. Hendon, J. Sun, M. Dincă, *Nat. Mater.* **2021**, *20*, 222.
- [15] R. W. Day, D. K. Bediako, M. Rezaee, L. R. Parent, G. Skorupskii, M. Q. Arguilla, C. H. Hendon, I. Stassen, N. C. Gianneschi, P. Kim, M. Dincă, *ACS Cent. Sci.* **2019**, *5*, 1959.
- [16] H. Qi, H. Sahabudeen, B. Liang, M. Položij, M. A. Addicoat, T. E. Gorelik, M. Hamsch, M. Mundszinger, S. W. Park, B. V. Lotsch, S. C. B. Mannsfeld, Z. Zheng, R. Dong, T. Heine, X. Feng, U. Kaiser, *Sci. Adv.* **2020**, *6*, eabb5976.
- [17] R. Dong, X. Feng, *Nat. Mater.* **2021**, *20*, 122.
- [18] M. Wang, H. Shi, P. Zhang, Z. Liao, M. Wang, H. Zhong, F. Schwotzer, A. S. Nia, E. Zschech, S. Zhou, S. Kaskel, R. Dong, X. Feng, *Adv. Funct. Mater.* **2020**, *30*, 2002664.
- [19] R. Dong, T. Zhang, X. Feng, *Chem. Rev.* **2018**, *118*, 6189.
- [20] R. Dong, M. Pfeiffermann, H. Liang, Z. Zheng, X. Zhu, J. Zhang, X. Feng, *Angew. Chem., Int. Ed.* **2015**, *54*, 12058.
- [21] G. Wu, J. Huang, Y. Zang, J. He, G. Xu, *J. Am. Chem. Soc.* **2017**, *139*, 1360.
- [22] N. Lahiri, N. Lotfizadeh, R. Tsuchikawa, V. V. Deshpande, J. Louie, *J. Am. Chem. Soc.* **2017**, *139*, 19.
- [23] B. Wang, Y. Luo, B. Liu, G. Duan, *ACS Appl. Mater. Interfaces* **2019**, *11*, 35935.
- [24] V. Rubio-Giménez, N. Almora-Barrios, G. Escorcía-Ariza, M. Galbiati, M. Sessolo, S. Tatay, C. Martí-Gastaldo, *Angew. Chem., Int. Ed.* **2018**, *57*, 15086.
- [25] M. G. Campbell, D. Sheberla, S. F. Liu, T. M. Swager, M. Dincă, *Angew. Chem., Int. Ed.* **2015**, *54*, 4349.
- [26] M. G. Campbell, S. F. Liu, T. M. Swager, M. Dincă, *J. Am. Chem. Soc.* **2015**, *137*, 13780.
- [27] M. S. Yao, X. J. Lv, Z. H. Fu, W. H. Li, W. H. Deng, G. D. Wu, G. Xu, *Angew. Chem., Int. Ed.* **2017**, *56*, 16510.
- [28] T. Takenaka, K. Ishihara, M. Roppongi, Y. Miao, Y. Mizukami, T. Makita, J. Tsurumi, S. Watanabe, J. Takeya, M. Yamashita, K. Torizuka, Y. Uwatoko, T. Sasaki, X. Huang, W. Xu, D. Zhu, N. Su, J. G. Cheng, T. Shibauchi, K. Hashimoto, *Sci. Adv.* **2021**, *7*, 3996.
- [29] Z. Chen, Y. Cui, Y. Jin, L. Liu, J. Yan, Y. Sun, Y. Zou, Y. Sun, W. Xu, D. Zhu, *J. Mater. Chem. C* **2020**, *8*, 8199.
- [30] M. Yu, R. Dong, X. Feng, *J. Am. Chem. Soc.* **2020**, *142*, 12903.
- [31] M. D. Allendorf, R. Dong, X. Feng, S. Kaskel, D. Matoga, V. Stavila, *Chem. Rev.* **2020**, *120*, 8581.
- [32] J. Park, A. C. Hinckley, Z. Huang, D. Feng, A. A. Yakovenko, M. Lee, S. Chen, X. Zou, Z. Bao, *J. Am. Chem. Soc.* **2018**, *140*, 14533.
- [33] J. H. Dou, L. Sun, Y. Ge, W. Li, C. H. Hendon, J. Li, S. Gul, J. Yano, E. A. Stach, M. Dincă, *J. Am. Chem. Soc.* **2017**, *139*, 13608.
- [34] Y. Cui, J. Yan, Z. Chen, J. Zhang, Y. Zou, Y. Sun, W. Xu, D. Zhu, *Adv. Sci.* **2019**, *6*, 1802235.
- [35] D. Sheberla, L. Sun, M. A. Blood-Forsythe, S. Er, C. R. Wade, C. K. Brozek, A. Aspuru-Guzik, M. Dincă, *J. Am. Chem. Soc.* **2014**, *136*, 8859.
- [36] Y. Cui, J. Yan, Z. Chen, W. Xing, C. Ye, X. Li, Y. Zou, Y. Sun, C. Liu, W. Xu, D. Zhu, *iScience* **2020**, *23*, 100812.
- [37] Z. Meng, K. A. Mirica, *Nano Res.* **2021**, *14*, 369.
- [38] Q. Zhao, S. H. Li, R. L. Chai, X. Ren, C. Zhang, *ACS Appl. Mater. Interfaces* **2020**, *12*, 7504.
- [39] H. Huang, Y. Zhao, Y. Bai, F. Li, Y. Zhang, Y. Chen, *Adv. Sci.* **2020**, *7*, 2000012.
- [40] C. Yang, R. Dong, M. Wang, P. S. Petkov, Z. Zhang, M. Wang, P. Han, M. Ballabio, S. A. Bräuninger, Z. Liao, J. Zhang, F. Schwotzer, E. Zschech, H. H. Klaus, E. Cánovas, S. Kaskel, M. Bonn, S. Zhou, T. Heine, X. Feng, *Nat. Commun.* **2019**, *10*, 3260.
- [41] Z. Meng, A. Aykanat, K. A. Mirica, *J. Am. Chem. Soc.* **2019**, *141*, 2046.
- [42] T. Kambe, R. Sakamoto, K. Hoshiko, K. Takada, M. Miyachi, J. H. Ryu, S. Sasaki, J. Kim, K. Nakazato, M. Takata, H. Nishihara, *J. Am. Chem. Soc.* **2013**, *135*, 2462.
- [43] M. A. Springer, T. J. Liu, A. Kuc, T. Heine, *Chem. Soc. Rev.* **2020**, *49*, 2007.
- [44] G. Chakraborty, I. H. Park, R. Medishetty, J. J. Vittal, *Chem. Rev.* **2021**, *121*, 3751.
- [45] L. P. Tang, L. M. Tang, D. Wang, H. X. Deng, K. Q. Chen, *J. Phys. Condens. Matter* **2018**, *30*, 465301.
- [46] L. P. Tang, L. M. Tang, H. Geng, Y. P. Yi, Z. Wei, K. Q. Chen, H. X. Deng, *Appl. Phys. Lett.* **2018**, *112*, 012101.
- [47] T. Kambe, R. Sakamoto, T. Kusamoto, T. Pal, N. Fukui, K. Hoshiko, T. Shimojima, Z. Wang, T. Hirahara, K. Ishizaka, S. Hasegawa, F. Liu, H. Nishihara, *J. Am. Chem. Soc.* **2014**, *136*, 14357.
- [48] M. K. Smith, K. A. Mirica, *J. Am. Chem. Soc.* **2017**, *139*, 16759.
- [49] R. Dong, Z. Zheng, D. C. Tranca, J. Zhang, N. Chandrasekhar, S. Liu, X. Zhuang, G. Seifert, X. Feng, *Chem. Eur. J.* **2017**, *23*, 2255.
- [50] X. Sun, K. H. Wu, R. Sakamoto, T. Kusamoto, H. Maeda, H. Nishihara, *Chem. Lett.* **2017**, *46*, 1072.
- [51] T. Chen, J. H. Dou, L. Yang, C. Sun, N. J. Libretto, G. Skorupskii, J. T. Miller, M. Dincă, *J. Am. Chem. Soc.* **2020**, *142*, 12367.

- [52] Z. Wang, G. Wang, H. Qi, M. Wang, M. Wang, S. W. Park, H. Wang, M. Yu, U. Kaiser, A. Fery, S. Zhou, R. Dong, X. Feng, *Chem. Sci.* **2020**, *11*, 7665.
- [53] M. Zhao, Y. Wang, Q. Ma, Y. Huang, X. Zhang, J. Ping, Z. Zhang, Q. Lu, Y. Yu, H. Xu, Y. Zhao, H. Zhang, *Adv. Mater.* **2015**, *27*, 7372.
- [54] L. Wang, H. Sahabudeen, T. Zhang, R. Dong, *npj 2D Mater. Appl.* **2018**, *2*, 26.
- [55] T. Pal, T. Kambe, T. Kusamoto, M. L. Foo, R. Matsuoka, R. Sakamoto, H. Nishihara, *Chempluschem* **2015**, *80*, 1255.
- [56] X. Huang, H. Li, Z. Tu, L. Liu, X. Wu, J. Chen, Y. Liang, Y. Zou, Y. Yi, J. Sun, W. Xu, D. Zhu, *J. Am. Chem. Soc.* **2018**, *140*, 15153.
- [57] A. J. Clough, N. M. Orchanian, J. M. Skelton, A. J. Neer, S. A. Howard, C. A. Downes, L. F. J. Piper, A. Walsh, B. C. Melot, S. C. Marinescu, *J. Am. Chem. Soc.* **2019**, *141*, 16323.
- [58] K. Yuan, T. Song, X. Zhu, B. Li, B. Han, L. Zheng, J. Li, X. Zhang, W. Hu, *Small* **2019**, *15*, 1804845.
- [59] Z. Wang, L. S. Walter, M. Wang, P. S. Petkov, B. Liang, H. Qi, N. N. Nguyen, M. Hamsch, H. Zhong, M. Wang, S. Park, L. Renn, K. Watanabe, T. Taniguchi, S. C. B. Mannsfeld, T. Heine, U. Kaiser, S. Zhou, R. T. Weitz, X. Feng, R. Dong, *J. Am. Chem. Soc.* **2021**, *143*, 13624.
- [60] M. Zhang, B. H. Zheng, J. Xu, N. Pan, J. Yu, M. Chen, H. Cao, *Chem. Commun.* **2018**, *54*, 13579.
- [61] Y. Chen, X. L. Gong, J. G. Gai, *Adv. Sci.* **2016**, *3*, 1500343.
- [62] L. A. Cao, M. S. Yao, H. J. Jiang, S. Kitagawa, X. L. Ye, W. H. Li, G. Xu, *J. Mater. Chem. A* **2020**, *8*, 9085.
- [63] X. Song, X. Wang, Y. Li, C. Zheng, B. Zhang, C. an Di, F. Li, C. Jin, W. Mi, L. Chen, W. Hu, *Angew. Chem. Int. Ed.* **2020**, *59*, 1118.
- [64] A. Mahringer, A. C. Jakowetz, J. M. Rotter, B. J. Bohn, J. K. Stolarczyk, J. Feldmann, T. Bein, D. D. Medina, *ACS Nano* **2019**, *13*, 6711.
- [65] Y. Liu, Y. Wei, M. Liu, Y. Bai, X. Wang, S. Shang, J. Chen, Y. Liu, *Angew. Chem., Int. Ed.* **2021**, *60*, 2887.
- [66] Y. Liu, Y. Wei, M. Liu, Y. Bai, X. Wang, S. Shang, C. Du, W. Gao, J. Chen, Y. Liu, *Adv. Mater.* **2021**, *33*, 2007741.
- [67] D. G. Ha, M. Rezaee, Y. Han, S. A. Siddiqui, R. W. Day, L. S. Xie, B. J. Modtland, D. A. Muller, J. Kong, P. Kim, M. Dincă, M. A. Baldo, *ACS Cent. Sci.* **2021**, *7*, 104.
- [68] I. Stassen, M. Styles, G. Greci, H. Van Gorp, W. Vanderlinden, S. De Feyter, P. Falcaro, D. De Vos, P. Vereecken, R. Ameloot, *Nat. Mater.* **2016**, *15*, 304.
- [69] Y. Chen, J. Liu, M. Zeng, F. Lu, T. Lv, Y. Chang, H. Lan, B. Wei, R. Sun, J. Gao, Z. Wang, L. Fu, *Nat. Commun.* **2020**, *11*, 3979.
- [70] M. Zeng, J. Liu, L. Zhou, R. G. Mendes, Y. Dong, M.-Y. Zhang, Z.-H. Cui, Z. Cai, Z. Zhang, D. Zhu, T. Yang, X. Li, J. Wang, L. Zhao, G. Chen, H. Jiang, M. H. Rummeli, H. Zhou, L. Fu, *Nat. Mater.* **2020**, *19*, 528.
- [71] J. Liu, M. Zeng, L. Wang, Y. Chen, Z. Xing, T. Zhang, Z. Liu, J. Zuo, F. Nan, R. G. Mendes, S. Chen, F. Ren, Q. Wang, M. H. Rummeli, L. Fu, *Small* **2016**, *12*, 5741.
- [72] Y. Chen, K. Liu, J. Liu, T. Lv, B. Wei, T. Zhang, M. Zeng, Z. Wang, L. Fu, *J. Am. Chem. Soc.* **2018**, *140*, 16392.
- [73] F. J. Claire, M. A. Solomos, J. Kim, G. Wang, M. A. Siegler, M. F. Crommie, T. J. Kempa, *Nat. Commun.* **2020**, *11*, 5524.
- [74] J. Ogle, N. Lahiri, C. Jaye, C. J. Tassone, D. A. Fischer, J. Louie, L. Whittaker-Brooks, *Adv. Funct. Mater.* **2021**, *31*, 2006920.
- [75] X. Du, J. Zhang, H. Wang, Z. Huang, A. Guo, L. Zhao, Y. Niu, X. Li, B. Wu, Y. Liu, *Mater. Chem. Front.* **2020**, *4*, 243.
- [76] Q. Jiang, C. Zhou, H. Meng, Y. Han, X. Shi, C. Zhan, R. Zhang, *J. Mater. Chem. A* **2020**, *8*, 15271.
- [77] M. Lischka, R. Dong, M. Wang, N. Martsinovich, M. Fritton, L. Grossmann, W. M. Heckl, X. Feng, M. Lackinger, *Chem. Eur. J.* **2019**, *25*, 1975.
- [78] X. Meng, E. Kolodzeiski, X. Huang, A. Timmer, B. Schulze Lammers, H. Y. Gao, H. Mönig, L. Liu, W. Xu, S. Amirjalayer, D. Zhu, H. Fuchs, *ChemNanoMat* **2020**, *6*, 1479.
- [79] Z. Gao, C. H. Hsu, J. Liu, F. C. Chuang, R. Zhang, B. Xia, H. Xu, L. Huang, Q. Jin, P. N. Liu, N. Lin, *Nanoscale* **2019**, *11*, 878.
- [80] R. Zhang, J. Liu, Y. Gao, M. Hua, B. Xia, P. Knecht, A. C. Papageorgiou, J. Reichert, J. V. Barth, H. Xu, L. Huang, N. Lin, *Angew. Chem., Int. Ed.* **2020**, *59*, 2669.
- [81] M. Ko, A. Aykanat, M. K. Smith, K. A. Mirica, *Sensors* **2017**, *17*, 2192.
- [82] M. K. Smith, K. E. Jensen, P. A. Pivak, K. A. Mirica, *Chem. Mater.* **2016**, *28*, 5264.
- [83] L. Mendecki, K. A. Mirica, *ACS Appl. Mater. Interfaces* **2018**, *10*, 19248.
- [84] X. Huang, S. Zhang, L. Liu, L. Yu, G. Chen, W. Xu, D. Zhu, *Angew. Chem., Int. Ed.* **2018**, *57*, 146.
- [85] L. E. Kreno, K. Leong, O. K. Farha, M. Allendorf, R. P. Van Duyne, J. T. Hupp, *Chem. Rev.* **2012**, *112*, 1105.
- [86] I. Stassen, J. H. Dou, C. Hendon, M. Dincă, *ACS Cent. Sci.* **2019**, *5*, 1425.
- [87] A. Tarasov, S. Zhang, M. Y. Tsai, P. M. Campbell, S. Graham, S. Barlow, S. R. Marder, E. M. Vogel, *Adv. Mater.* **2015**, *27*, 1175.
- [88] M. S. Yao, J. J. Zheng, A. Q. Wu, G. Xu, S. S. Nagarkar, G. Zhang, M. Tsujimoto, S. Sakaki, S. Horike, K. Otake, S. Kitagawa, *Angew. Chem., Int. Ed.* **2020**, *59*, 172.
- [89] B. Hoppe, K. D. J. Hindricks, D. P. Warwas, H. A. Schulze, A. Mohmeyer, T. J. Pinkvos, S. Zailskas, M. R. Krey, C. Belke, S. König, M. Fröba, R. J. Haug, P. Behrens, *CrystEngComm* **2018**, *20*, 6458.
- [90] M. Wang, Z. Zhang, H. Zhong, X. Huang, W. Li, M. Hamsch, P. Zhang, Z. Wang, P. St. Petkov, T. Heine, S. C. B. Mannsfeld, X. Feng, R. Dong, *Angew. Chem., Int. Ed.* **2021**, *60*, 18666.
- [91] X. Zhang, Y. Zhou, B. Cui, M. Zhao, F. Liu, *Nano Lett.* **2017**, *17*, 6166.
- [92] S. Liu, Y. C. Wang, C. M. Chang, T. Yasuda, N. Fukui, H. Maeda, P. Long, K. Nakazato, W. Bin Jian, W. Xie, K. Tsukagoshi, H. Nishihara, *Nanoscale* **2020**, *12*, 6983.
- [93] Z. Jin, J. Yan, X. Huang, W. Xu, S. Yang, D. Zhu, J. Wang, *Nano Energy* **2017**, *40*, 376.



Jinxin Liu received his B.S. degree in chemistry (2015) from Wuhan University and completed his Ph.D. in physical chemistry (2020) under the supervision of Prof. Lei Fu at the Laboratory of Advanced Nanomaterials of Wuhan University. Currently, he joined Prof. Xinliang Feng's group as a postdoctoral researcher at the Center for Advancing Electronics Dresden and Technische Universität Dresden to work on controllable chemical vapor deposition growth of 2D conductive metal–organic frameworks.



Yunxu Chen received her B.S. from Xinyang Normal University in 2015, and completed her Ph.D studies under the supervision of Prof. Lei Fu in the College of Chemistry and Molecular Sciences at Wuhan University. Currently, she joined Prof. Xinliang Feng's group as a postdoctoral researcher at Technische Universität Dresden. Her current research interests are chemical vapor deposition growth of two-dimensional polymers.



Xinliang Feng is a full professor and has been the head of the Chair for Molecular Functional Materials at Technische Universität Dresden since 2014. His current scientific interests include organic synthetic methodology, organic synthesis, and supramolecular chemistry of π -conjugated systems, bottom-up synthesis of graphene and graphene nanoribbons, electrochemical exfoliation of 2D crystals, 2D polymers, and supramolecular polymers as well as 2D carbon-rich conjugated polymers for optoelectronic applications, energy storage and conversion, and new energy devices and technologies. He has published more than 480 research articles, which have attracted more than 52,000 citations with an H-index of 109.



Renhao Dong received his bachelor's degree in chemistry in 2008 and then a doctor degree in physical chemistry in 2013 from Shandong University (SDU). After that, he joined Max Planck Institute for Polymer Research and then Technische Universität Dresden (TUD) for postdoctoral research. Since 2017, he leads an independent research group at TUD. Since 2020, he runs a TUD Young Investigator program. His current scientific interests focus on chemistry of organic 2D crystal materials such as 2D conjugated polymers, 2D covalent organic frameworks, and 2D metal-organic frameworks, as well as their functions in electronics and energy storage/conversion.